Supplementary Materials for

Strain Stabilized Nickel Hydroxide Nanoribbons for Efficient Water Splitting

Authors: X. P. Wang[1#], H. J. Wu[1#], S. B. Xi[2], W. S. V. Lee[1,] J. Zhang[3], Z. H. Wu[3], J. O. Wang[3], T. D. Hu[3], L. M. Liu[4], Y. Han[4], S. W. Chee[5], S. C. Ning,[1] U. Mirsaidov[6], Z. B. Wang[7], Y.W. Zhang[8], A. Borgna[2], J. Wang[1], Y. H. Du[2*], Z. G. Yu[7*], S. J. Pennycook[1*] and J. M. Xue[1*]

Affiliations:

[1] Department of Materials Science and Engineering, National University of Singapore, Singapore, 117575.

[2] Institute of Chemical and Engineering Sciences, Agency for Science, Technology and Research, Singapore, 627833.

[3] Beijing Synchrotron Radiation Facility, Institute of High Energy Physics, Chinese Academy of Sciences, Beijing 100049, People's Republic of China.

[4] Advanced Membranes and Porous Materials Center, Physical Science and Engineering Division, King Abdullah University of Science and Technology, Thuwal 23955-6900, Saudi Arabia.

[5] Centre for Bioimaging Sciences, 14 Science Drive 4, National University of Singapore, Singapore 117557, Singapore.

[6] Department of Physics, National University of Singapore, Singapore 117551, Singapore.

[7] School of Chemistry and Chemical Engineering, Harbin Institute of Technology, Heilongjiang Sheng 150006, China.

[8] Institute of High Performance Computing, Agency for Science, Technology and Research, Singapore, 138632.

# Equal contribution.

*Correspondence to: msexuejm@nus.edu.sg (J.M. Xue); steve.pennycook@nus.edu.sg (S.J. Pennycook); yuzg@ihpc.a-star.edu.sg (Z.G. Yu); du_yonghua@ices.a-star.edu.sg (Y.H. Du).

This PDF file includes:

Materials and Methods

Chemicals

Nickel sulfate ($NiSO_4$, CAS: 10101-97-0, 99%), boric acid (H_3BO_3, CAS: 10043-35-3, 99.5%), nickel nitrate hexahydrate ($Ni(NO_3)_2 \cdot 6H_2O$, CAS: 13478-00-7, 99%), hexamethylenetetramine (HMT, CAS: 10043-35-3, 99.5%). All the chemicals were used without further purification.

Synthesis of NR-$Ni(OH)_2$

(1) Electrodeposition of Ni onto carbon cloth. First, the carbon cloth (CC) was heat treated at 500˚C for 1 hour in air to increase its wettability. Ni was then coated on the CC (1*2 cm^2) through electrodeposition. With the CC acting as the working electrode and Pt as the counter electrode, a constant current of -10 mA cm^{-2} was obtained for 1.5 hours. The electrodeposition solution contained 0.15 M $NiSO_4$ and 0.6 M H_3BO_4. After electrodeposition, it was washed using DI water, followed by drying 60 ˚C in air for 4 hours.

(2) Formation of NiS_2. The obtained Ni-coated CC sample was then heat treated with sulfur at 400 ˚C under Ar atmosphere for 1 hour, as shown in the following figure. After cooling down to room temperature, the sample was washed using deionized (DI) water and then dried at 80 ˚C for 1 hour.

(3) Electro-oxidation of NiS_2 in KOH solution. Electro-oxidation was performed using a three-electrode configuration, with NiS_2 (attached onto carbon cloth), Pt, and Hg/HgO electrodes as working electrode, counter electrode, and reference electrode, respectively, under a constant current of 10 mA cm^{-2} for about 8 hours.

(4) Collection of NR-$Ni(OH)_2$ powder. After complete electro-oxidation, the sample was immersed into ethanol for more than 30 minutes to allow the reduction from NR-NiOOH to NR-$Ni(OH)_2$. This was followed by a sonication process to collect the NR-$Ni(OH)_2$ from the carbon cloth. The sonication and washing processes were repeated 9 times, to ensure there was no carbon left in the NR-$Ni(OH)_2$. The sample was dried at 60 ˚C for 10 hours.

Preparation of conventional β-$Ni(OH)_2$ electrode

Carbon cloth (CC) was heat-treated at 500˚C for 1 hour in air to increase its wettability. The deionized (DI) water was used to clean the CC several times. The cleaned CC (1cm*2cm) was immersed into 30 mL aqueous solution containing 5 mmol $Ni(NO_3)_2 \cdot 6H_2O$ and 10 mmol HMT. Then, the aqueous solution and CC were transferred into a teflon-lined stainless-steel autoclave and maintained at 100˚C for 10 hours. The prepared samples were washed using DI water, and then dried at 60˚C in air for 6 hours.

Characterization

TEM and STEM

The samples were dispersed in ethanol first. A droplet of the suspension was transferred onto carbon-coated copper grids using micropipettes and then dried under ambient condition. Transmission electron microscopy (TEM) using a JEOL 2010F at 200 kV was used to characterize the NiS_2 sample. Scanning transmission electron microscopy (STEM) and electron energy loss spectroscopy (EELS) studies were conducted using a JEOL ARM200F atomic resolution analytical electron microscope equipped with a cold field-emission gun, a new ASCOR 5th order aberration corrector and Gatan Quantum ER spectrometer. The electron beam dose is adjustable with probe size. Low-dose STEM was performed using the smallest probe size (10C) at 200 kV, whose electron density is ~1% of that of the normal probe size. Low-dose TEM images were acquired on an uncorrected FEI Titan 80–300 electron microscope by a Gatan K2 direct-detection camera operated in electron-counting mode (camera counting frame rate of 400 fps (frames per second) at 4 k × 4 k resolution) with a final image output rate of 40 fps at 4 k × 4 k resolution. The dose rate is ultralow 2 e/px/s and the total dose is ~56 e/A^2. The cooling experiment was done on a Gatan cooling holder in a FEI Tecnai TF20 with a Gatan K2 camera. The samples for STEM and TEM observation and SR-XRD came from the same batch of materials.

X-ray absorption fine structure

The *operando* and conventional Ni *K*-edge X-ray absorption fine structure (XAFS) data were collected at the 1W1B beamline of Beijing Synchrotron Radiation Facility (BSRF) of the Institute of High Energy Physics, Chinese Academy of Sciences and the XAFCA beamline at the Singapore Synchrotron Light Source (SSLS) under transmission mode. The storage ring of

BSRF is running at 2.5 GeV with electron current of 200 mA under top-up mode. The storage ring of SSLS is running at 0.7 GeV with electron current of about 250 mA. Energy calibrations were carried out using standard Ni foil.

XAFS Analysis

The IFEFFIT package (*6*) was implemented for the X-ray absorption fine structure (XAFS) data processing. Athena is used for the energy calibration, background removal, Fourier Transform (FT) and X-ray extended near-edge structure (XANES) linear combination fitting (LCF). For the FT, the k weight is 3 and data range is 2-10 $Å^{-1}$. The window function is Hanning. For the XANES LCF, the data range for the fitting is 8328-8448 eV. Artemis is used to do the extended XAFS (EXAFS) fitting. The EXAFS fitting results, including the coordination number, bond length and the Debye-Waller factor are provided in Table S1.

Near-edge X-ray absorption fine structure

Near-edge X-ray absorption fine structure (NEXAFS) spectra were measured at the 4B9B beamline of BSRF. The Ni L_2, L_3 edge NEXAFS spectra was collected in total electron yield mode with a photon energy resolution of 350 meV. The photon energy was calibrated using the characteristic intensity dip at 284.4 eV from the contamination carbon of the beamline optical components. All NEXAFS spectra are normalized to the incident photon intensity (I_0) monitored by the focusing mirror.

Synchrotron radiation X-ray diffraction

The synchrotron radiation X-ray diffraction (SR-XRD) experiment was performed at beamline 4B9A, 1W1A and 4W2 of BSRF. For 4B9A and 1W1A. The incident X-ray is monochromized to 0.154 nm using a double-crystal monochromator of Si (111). Note: for 4W2, the incident x-ray wavelength is 0.6199 nm. Data was collected by a PILATUS detector. The detector calibration was carried out with a standard CeO_2 powder. Data is converted based on 0.154 nm incident wavelength.

Electrochemical Measurement

Electrochemical measurements were performed using a three-electrode system connected to an electrochemical workstation (VMP3, Bio-logic Inc) with built-in electrochemical impedance spectroscopy (EIS) analyzer. The working electrode was the sample after electro-oxidation of NiS_2 8 hours (Electro-oxidation of NiS_2 in KOH solution sample), with the size of 1.0*1.0 cm. The reference electrode is a Hg/HgO electrode, which was calibrated through the method below. The counter electrode material was Pt.

Cyclic voltammetry (CV) measurement at 10 mV/s were performed for 3 cycles, before recording linear scan voltammetry (LSV). Polarization curves are measured from LSV with 0.1 mV/s, with 90% *iR* correction. The geometric area used in this work was from one side. The EIS spectra was conducted in static solution at 0V (vs Hg/HgO). The frequency scan ranges from 100 kHZ to 100 Hz. All the electrochemical measurements were performed at ambient temperature (22˚C).

Calibration of the reference electrode

The calibration of the Hg/HgO reference electrode was conducted in a standard three-electrode system (*7*). 1 M KOH solution was pre-purged with Grade 4 H_2 for at least 10 hours, then continued during the whole calibration process. The Hg/HgO electrode acts as the reference electrode, with Pt electrodes as working and counter electrode. LSV runs at about +/- 100 mV between hydrogen evolution and oxidation, as shown in Fig. S25.

ICP measurement

Sample was digested with HNO3/HCl (1:3) on hotplate and top up to 10ml with H_2O. Clear solution was observed prior to analysis.

Theoretical Calculations

NR-Ni$(OH)_2$ and NR-NiOOH structure simulation

All the simulated structures were carried out using density functional theory (DFT). Calculation of the NR-Ni$(OH)_2$ structure model was based on the optimized NR-NiOOH model.

NiOOH monolayer structure optimization. The bulk β-NiOOH structure (Fig. S1a) was optimized using the density functional theory (DFT) within the local-spin-polarized density approximations (LSDA+U, $^{U_{eff}} = 5.3\ eV$). The projector augmented-wave (PAW) pseudopotential planewave method was implemented in the VASP code (*2, 3*). For the PAW pseudopotential, $3d^8 4s^2$, $2s^2 2p^4$ and $1s^1$ were treated as valence electrons for Ni, O and H atoms, respectively. A 12×12×10 Monkhorst-Pack (MP) k-point grid was used for β-NiOOH unit cells geometry optimization calculations. Good convergence was obtained with these parameters, and the total energy was converged to 1×10^{-6} eV per atom. Energy convergence with respect to the plane wave cutoff was tested by varying the setting between 300 and 600 eV, and the convergence to within 10 meV was achieved with a cutoff energy of 500 eV for all calculations.

Then, the number of the β-NiOOH layer was reduced into one. The monolayer NiOOH structure was optimized using the same DFT calculation of the bulk β-NiOOH structure optimization. The optimized monolayer NiOOH structure could be seen in Fig. S1 b and c.

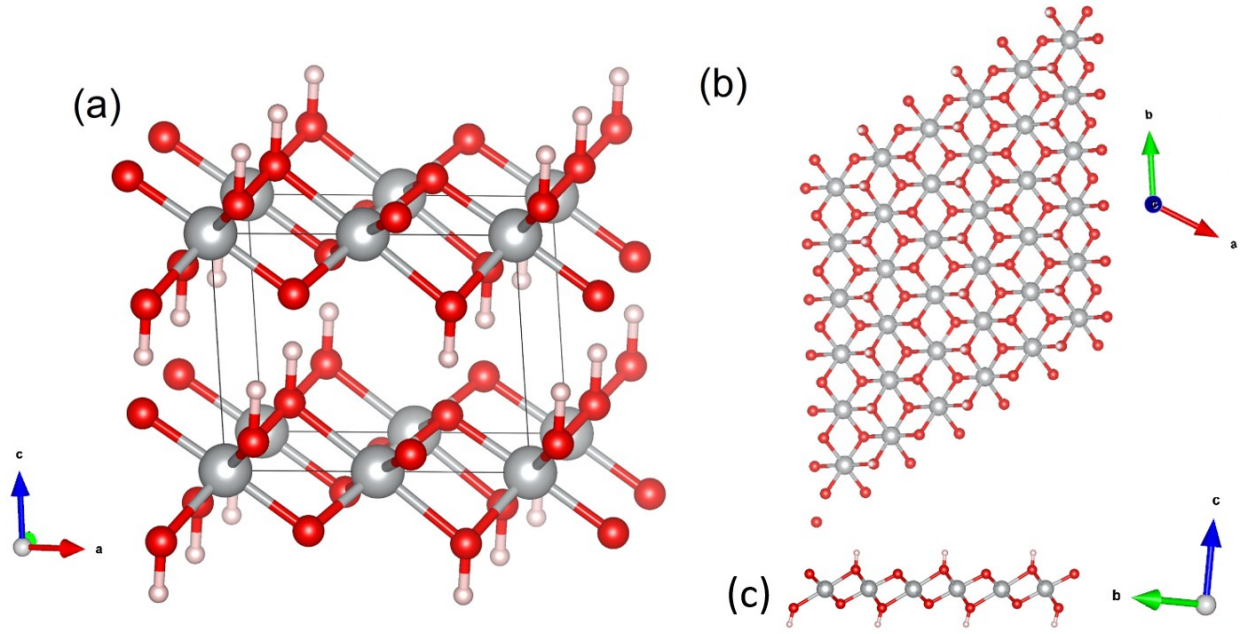

Fig. S1. (a) Optimized structure model for bulk β-NiOOH, (b) and (c) optimized structure model for monolayer NiOOH.

NR-NiOOH structure optimization. Based on the optimized NiOOH monolayer structure, NR-NiOOH models were constructed by cutting along the x-direction (XR) with alternating O and Ni atoms (zigzag edge) or along the y-direction (YR) with mixed O and Ni atoms (armchair edge), as seen the Fig. S2. Then, the stabilities of these NR-NiOOH models were explored. It should be noted that no chemical functionalization, such as hydrogenation, was considered.

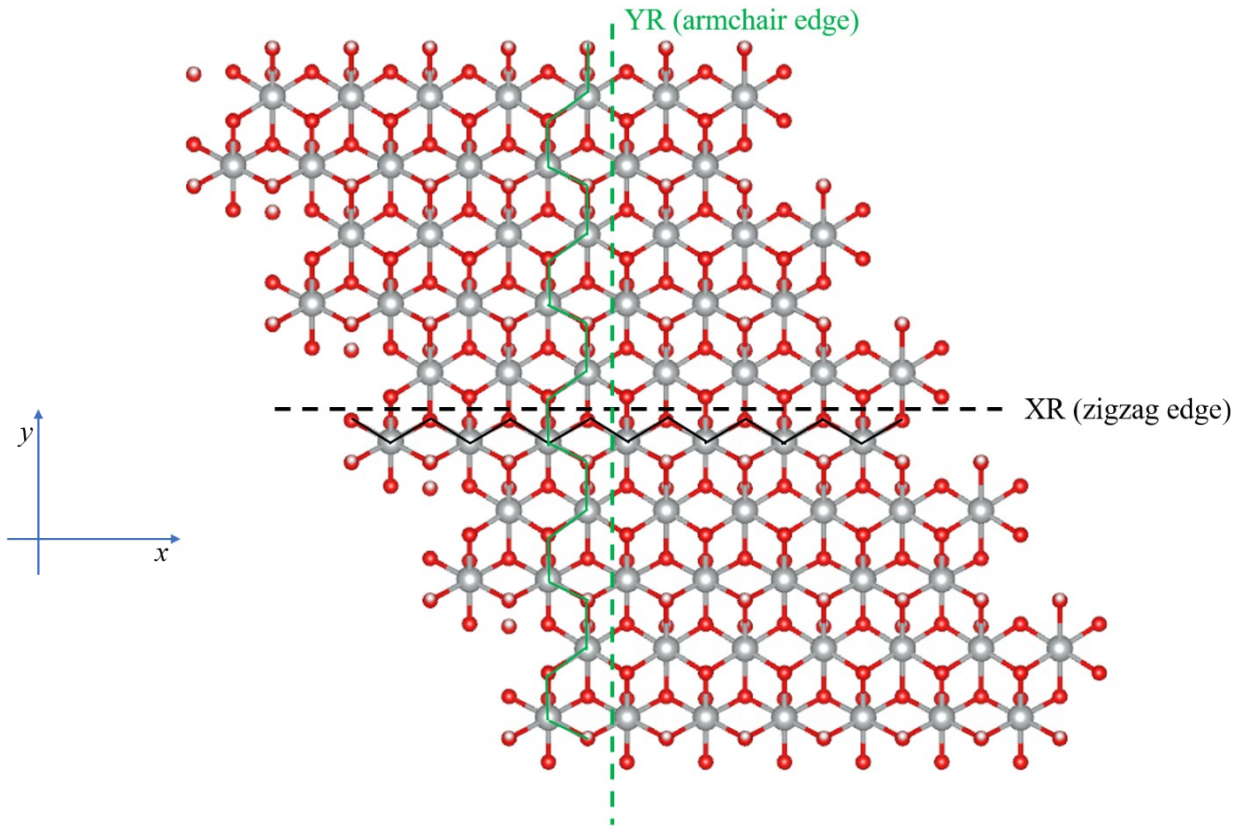

Fig. S2. The structure model for the XR and YR cutting.

For YR-series and XR-series, two different NR terminations were investigated: O termination with anti-symmetric edge (denoted –AS) and OH termination with symmetric edge (denoted –S). Then their ground-state energies were calculated, constraining the NR length to one unit cell. The distance between NR and its neighboring images is set to 20 Å and periodic boundary conditions (PBCs) are employed.

The edge energy (E_{edge}) is the indication of the structure stability, and was calculated from:

$$E_{edge} = (E_{NR} - nE_{NiOOH} - n_{Ni}\mu_{Ni} - n_O\mu_O - n_H\mu_H)/2L,$$

where, E_{NR} is the total energy of NiOOH NR, and E_{NiOOH} is the energy of the monolayer NiOOH unit cell, n is the number of NiOOH units in the structure model, L is the length, and $n_{Ni,O,H}$ and

$\mu_{Ni,O,H}$ are the numbers of extra Ni, O or H, and their chemical potentials, respectively. For monolayer NiOOH, at equilibrium $\mu_{Ni} + \mu_O + \mu_H = \mu_{NiOOH}$, where μ_{NiOOH} is the chemical potential of NiOOH. The calculated edge energies of the four types are shown in the following figure. It can be seen that, XR-S NR-Ni(OH)$_2$ with 13 Ni, 26 O and 14 H atoms is the most stable structure model, as seen in Fig. S3. In the next step, the NR-Ni(OH)$_2$ was calculated based on the XR-S NR-NiOOH.

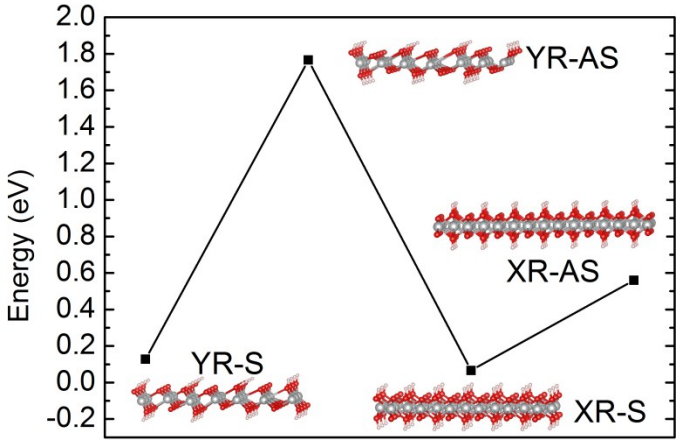

Fig. S3. The calculated edge energies of different types of NR-NiOOH structure models.

Calculation of the theoretical OER activity

All the calculations were carried out using density functional theory (DFT) with the generalized Perdew-Burke-Ernzerhof (PBE) (*1*), and the projector augmented-wave (PAW) pseudopotential planewave method was implemented in the VASP code (*2, 3*). For the PAW pseudopotential, $3d^8 4s^2$, $2s^2 2p^4$ and $1s^1$ were treated as valence electrons for Ni, O and H atoms, respectively.

The OER calculations were studied in detail in the following four electron reaction paths(*4*):

$$H_2O(l) + * \rightarrow OH^* + (H^+ + e^-) \quad (1)$$

$$OH^* \rightarrow O^* + (H^+ + e^-) \quad (2)$$

$$O^* + H_2O(l) \rightarrow OOH^* + (H^+ + e^-) \quad (3)$$

$$OOH^* \rightarrow * + O_2(g) + (H^+ + e^-) \quad (4)$$

where * strands for an active site on the surface, (l) and (g) denote the liquid and the gas phases, respectively. O^*, OH^* and OOH^* are the adsorbed intermediates. It was reported that the potential-determining step could either be the formation of O^* from OH^* (step 2) or the transformation of O^* to OOH^* (step 3), and the overpotential of the OER process could be calculated by examining the reaction free energies of different elementary steps using reported methods (*4*).

To obtain the rate-limiting step of OER on both models, the adsorption energy of O^*, OH^* and OOH^* were calculated. The adsorption energies were calculated from DFT simulations based on:

$$\Delta E_{OH^*} = E(OH^*) - E(*) - (E_{H_2O} - {}^1/_2 E_{H_2}) \quad (5)$$

$$\Delta E_{OOH^*} = E(OOH^*) - E(*) - (2E_{H_2O} - {}^3/_2 E_{H_2}) \quad (6)$$

$$\Delta E_{O^*} = E(O^*) - E(*) - (E_{H_2O} - E_{H_2}). \quad (7)$$

Here, $E(OH^*)$, $E(OOH^*)$, $E(O^*)$ and $E(*)$ are the ground state energies of models with the adsorbed intermediates of OH^*, OOH^*, O^* respectively. E_{H_2O} and E_{H_2} are the computed DFT energies of H_2O and H_2 molecules in the gas phase. For adsorption energy calculations, corrections resulting from the zero point energy (ZPE) and entropy were considered. Therefore, we can calculate reaction free energies based on the calculated adsorption energies by the following equation (*4*):

$$\Delta G_{ads} = \Delta E + \Delta ZPE - T\Delta S \quad (8)$$

where *T* is the temperature and ΔS is the entropy change. It should be noted that only the standard molar vibrational entropy based on the reported method was considered (*5*). In this study, the solvent correction to the adsorbed intermediates was ignored. For each step, the reaction free energy was defined as the difference between free energies without and with adsorbed intermediates (*4*).

The first step is to split the water molecule on the active site and release a proton and an electron (Eq. 1):

$$\Delta G_1 = E(OH^*) - E(*) - \left(E_{H_2O} - {}^1/_2 E_{H_2}\right) + (\Delta ZPE - T\Delta S) + k_b T \ln a_{H^+} - eU \quad (9)$$

The second step is the oxidation of OH^* species into O^* with release of a proton and an electron (Eq. 2):

$$\Delta G_2 = E(O^*) - E(OH^*) + {}^1/_2 E_{H_2} + (\Delta ZPE - T\Delta S) + k_b T \ln a_{H^+} - eU \quad (10)$$

The third step is to split the water molecule on top of oxygen and release a proton and an electron (Eq. 3):

$$\Delta G_3 = E(OOH^*) - E(O^*) - \left(E_{H_2O} - {}^1/_2 E_{H_2}\right) + (\Delta ZPE - T\Delta S) + k_B T \ln a_{H^+} - eU \quad (11)$$

The forth step is the evolution of oxygen (Eq. 4):

$$\Delta G_4 = 4.92 - (\Delta G_1 + \Delta G_2 + \Delta G_3) \quad (12)$$

Here, k_B is Boltzmann constant, and a_{H^+} represents the activity of protons. U is the potential at the electrode and *e* is the charge transferred. For an ideal catalyst, all four steps have the same reaction free energy of 1.23 eV at zero potential (4.92 eV/4), and the reaction free energy will be reduced to zero at an equilibrium potential of U=1.23 V. For simplicity, in this study we restricted the pH to 0. The calculated free energy based on equations (9)-(12) can be used to estimate the overpotential η^{OER} based on the following equation:

$$\eta^{OER} = max\{\Delta G_1, \Delta G_2, \Delta G_3, \Delta G_4\}/e - 1.23 \quad (13)$$

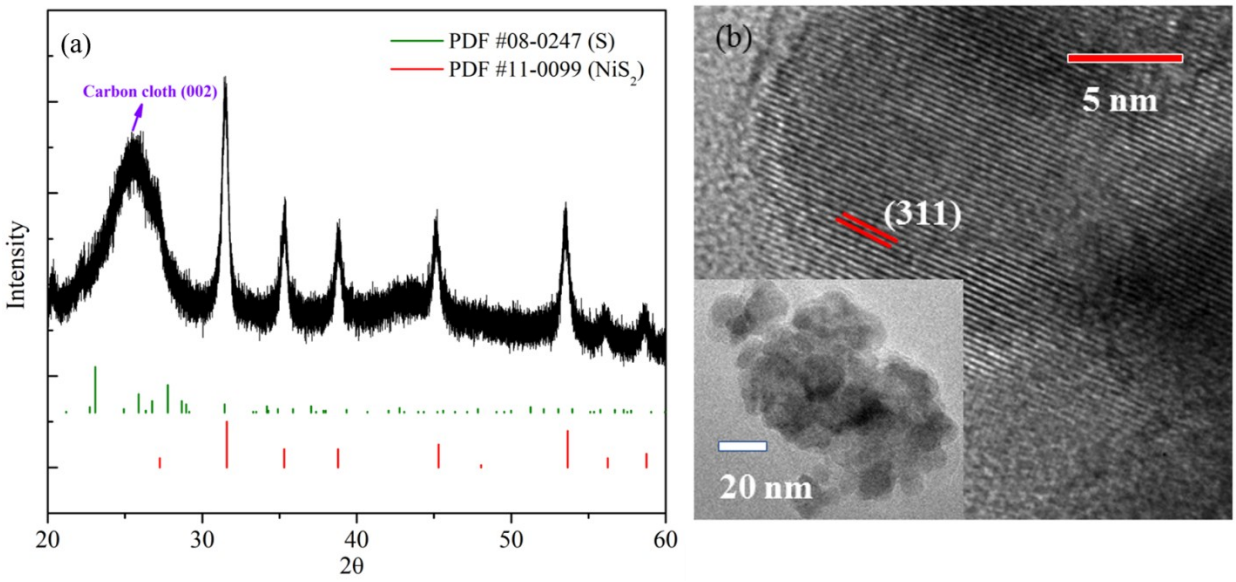

Fig. S4. XRD (a) and TEM (b) analysis of NiS_2. The broad peak ranging from 20 to 30° (2Θ) corresponds to the substrate carbon cloth (002) peak. In the HRTEM image, the lattice spacing is about 1.7 nm, matching well with the NiS_2 (311) plane.

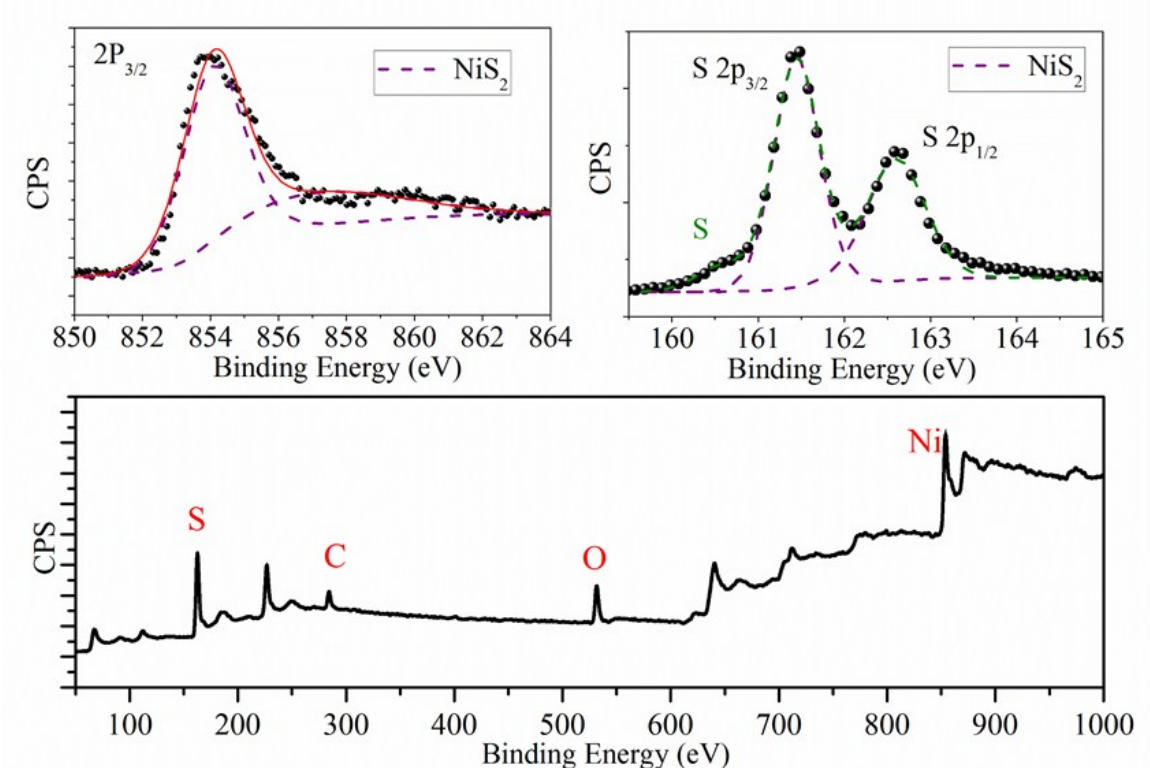

Fig. S5. XPS analysis of NiS_2. From Ni $2P_{3/2}$ and S $2P_{3/2,\ 1/2}$ spectra, it is confirmed that NiS_2 was successfully formed.

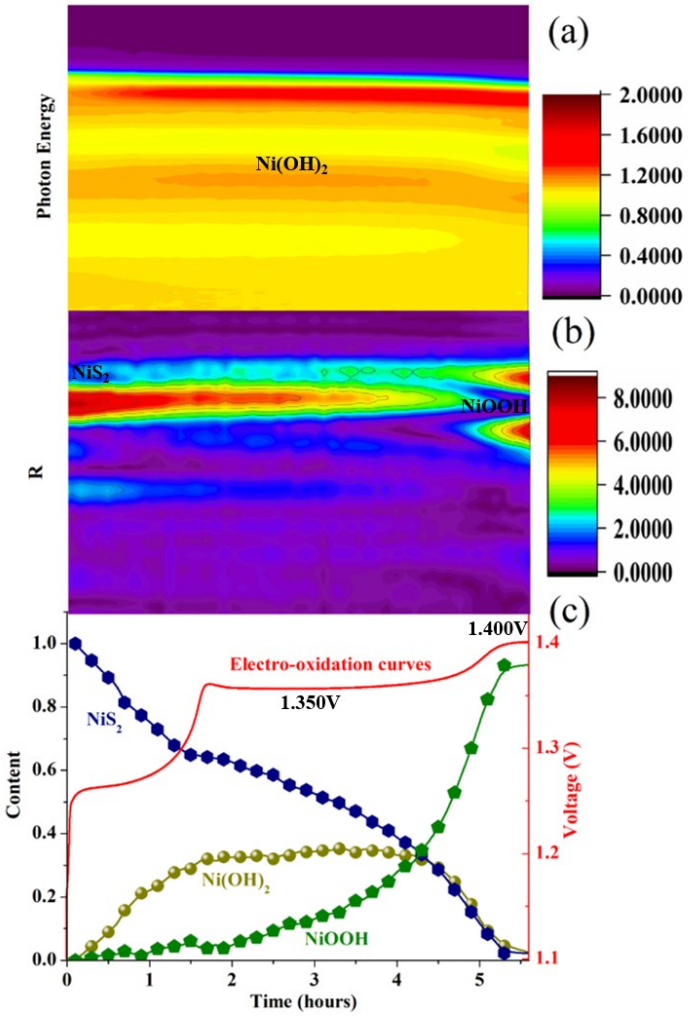

Fig. S6. *Operando* XAFS for electro-oxidation of NiS_2 and structural identification via X-ray absorption fine structure and synchrotron radiation X-ray diffraction. (a) Projections of *operando* XANES. (b) Projections of *operando* Fourier-transformed EXAFS spectra. (c) Composition variation among NiS_2, $Ni(OH)_2$ and NiOOH during electro-oxidation.

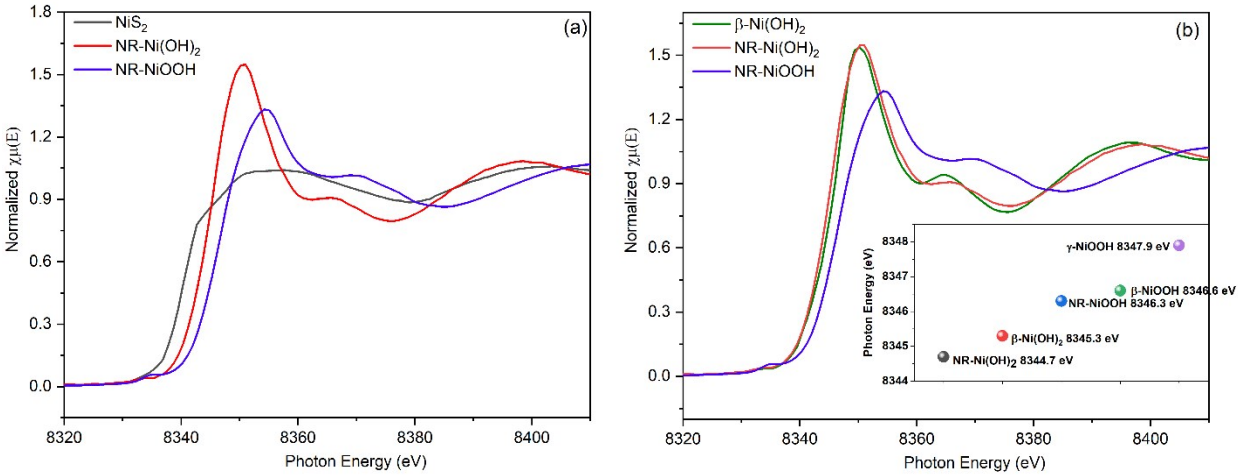

Fig. S7. (a) Ni *K* edge XANES spectra of NiS_2, $Ni(OH)_2$ and NiOOH; (b) XANES spectra of β-$Ni(OH)_2$, NR-$Ni(OH)_2$ and NR-NiOOH. (Inset) Edge energy at half jump height of β-$Ni(OH)_2$, NR-$Ni(OH)_2$, NR-NiOOH, β-NiOOH and γ-NiOOH. In order to ensure the complete reduction of NiOOH, the edge energy at half jump height (measured at half height $F/I_0 = 0.5$) of the samples including the traditional β-$Ni(OH)_2$, NR-NiOOH and NR-$Ni(OH)_2$ were used for comparison, suggesting that the NR-NiOOH was completely reduced into NR-$Ni(OH)_2$. At the same time, the XANES spectra indicates the edge position of NR-NiOOH is 8346.3 eV, which is smaller than β-NiOOH (8346.6 eV) (Inset of Fig. S7). This means, the mean Ni valence of NR-NiOOH is less than 3 (*64*).

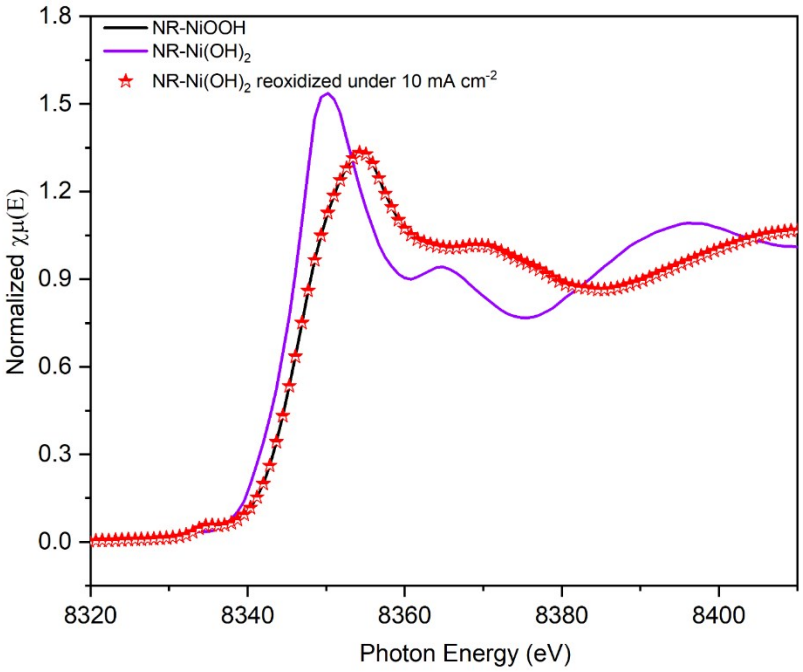

Fig. S8. XANES spectra of NR-Ni(OH)$_2$, NR-NiOOH and NR-Ni(OH)$_2$ re-oxidized sample. It is observed that these two curves are overlapped completely, which indicated that there was no significant structure change between NR-Ni(OH)$_2$ and NR-NiOOH.

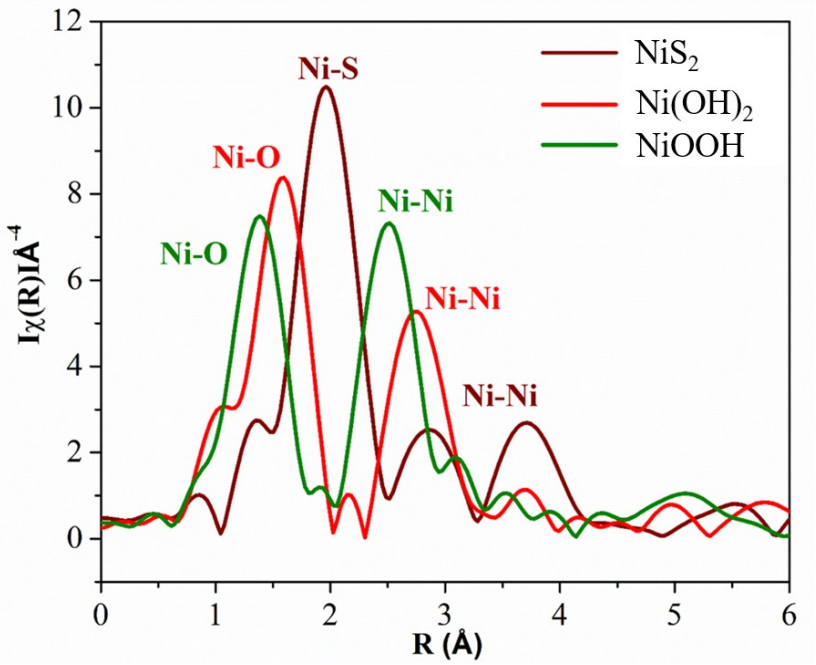

Fig. S9. Fourier-transformed EXAFS spectra of NiS_2, $Ni(OH)_2$ and NiOOH. No Ni-S bond could be seen in the $Ni(OH)_2$ and NiOOH samples. The EXAFS fitting results, including the coordination number, bond length and the Debye-Waller factor are provided in Table S1.

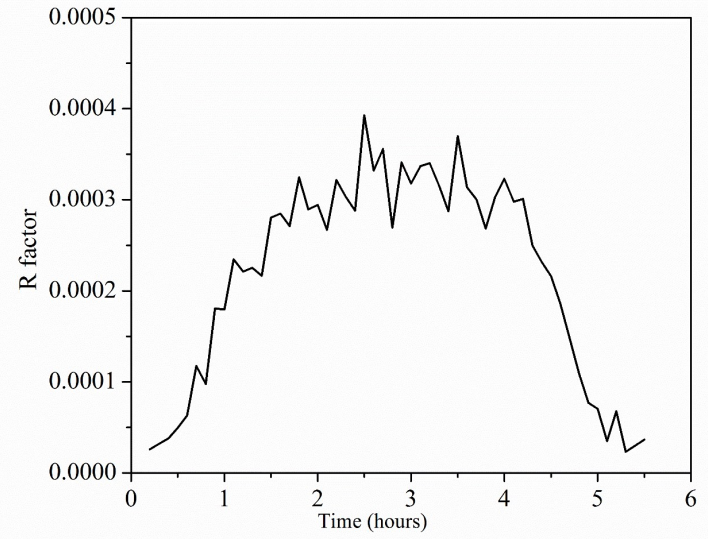

Fig. S10. The R factor of the linear combination fitting results. The small R factors (<0.0005) show that the fitting results are reliable.

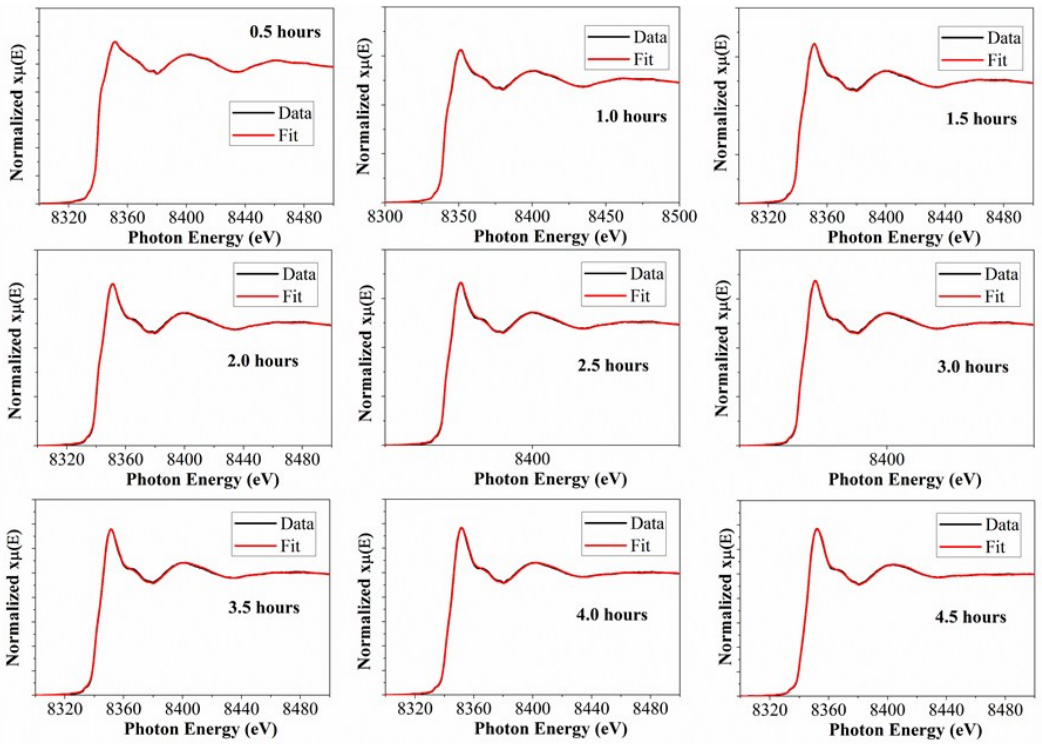

Fig. S11. Selected LCF fitting curves for the *Operando* XANES. Data was collected at the 1W1B beamline of the Beijing Synchrotron Radiation Facility. The well-fitted results in each stage show that the LCF fitting results are reliable.

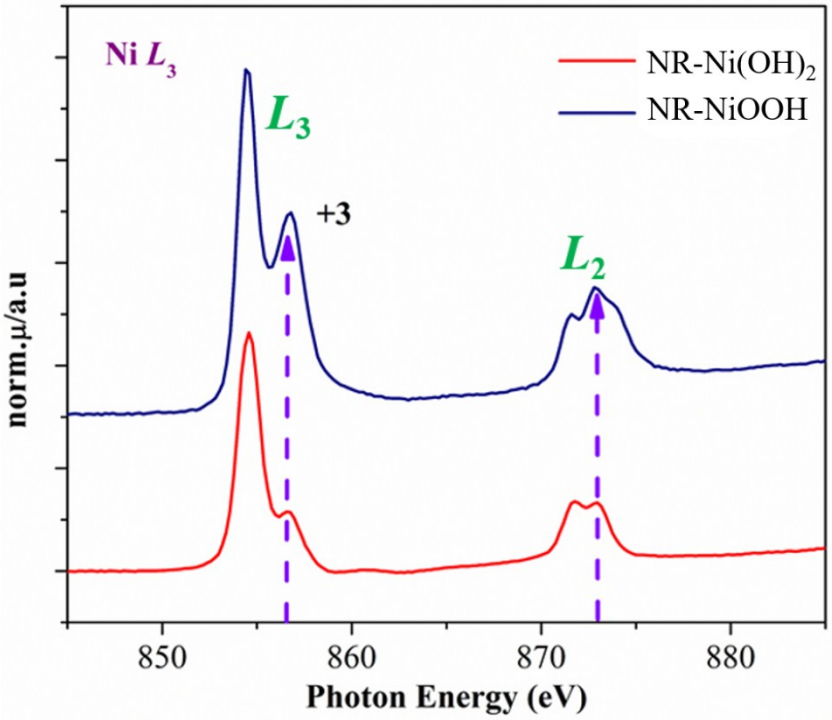

Fig. S12. Ni L_2 L_3, edge NEXAS spectra of NR-Ni(OH)$_2$ and NR-NiOOH. This confirms the increase in Ni valence when NR-Ni(OH)$_2$ is oxidized into NR-NiOOH.

Summary of Figs. S6-12: The projections of operando XANES and Fourier-transformed EXAFS spectra demonstrate the co-existence of NiS_2, Ni(OH)$_2$, and NiOOH during the electro-oxidation process. XANES linear combination fitting (LCF) was then carried out to analyze the phase transitions among NiS_2, Ni(OH)$_2$ and NiOOH (standard samples for LCF are shown in Figs. S7 and S9). The fitting results clearly show phase transitions from NiS_2 to Ni(OH)$_2$ and then to NiOOH (R factors and selected fitting curves can be seen in Figs. S10-11), which accords well with the appearance of three plateaus observed in the electro-oxidation curves. At the last plateaus staring from the potential 1.400 V vs RHE (1.391 V vs RHE after *iR* correction, corresponding to overpotential of 161 mV), all NiS_2 and Ni(OH)$_2$ were consumed, with only NiOOH left. To confirm the valence state of Ni ion at this stage, Ni L_2 L_3 edge NEXAS spectra of the sample were collected, confirming the presence of NiOOH, and suggesting that the oxidation reaction from Ni(OH)$_2$ to NiOOH had been completed (Fig. S12).

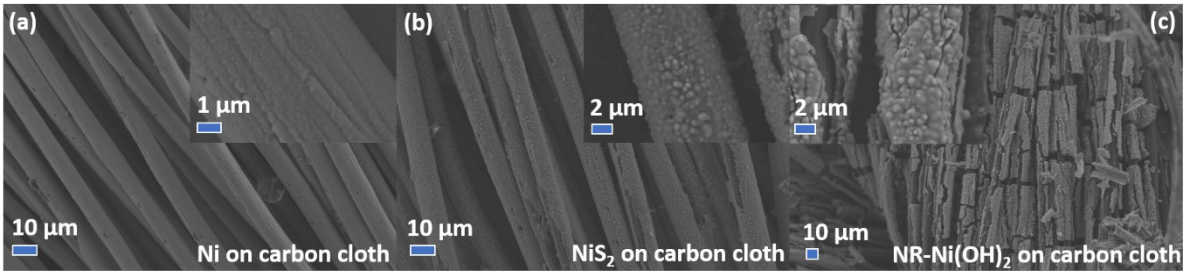

Fig. S13. SEM images of Ni (a), NiS_2 (b) and NR-$Ni(OH)_2$ on carbon cloth. It was observed that the particle size was increased slightly when Ni became NiS_2 upon sulfurization. The particle morphology was greatly changed when NiS_2 was transformed into NR-$Ni(OH)_2$ upon electro-oxidation.

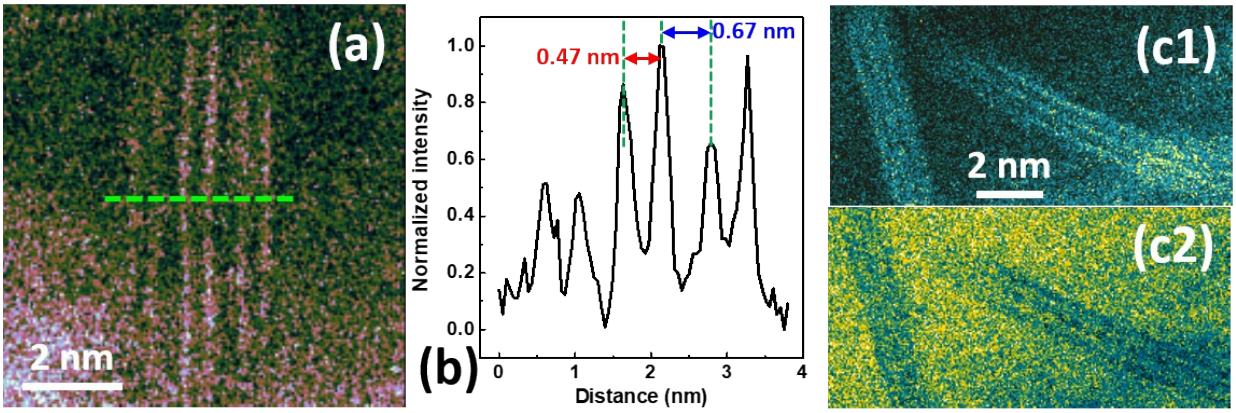

Fig. S14. Atomically-resolved STEM HAADF images. (a) Enlarged STEM HAADF image showing a batch of double layers, aligning together. (b) Intensity profile along the line marked in (a). (c1, c2) Enlarged STEM HAADF images showing two triple layers, not aligned.

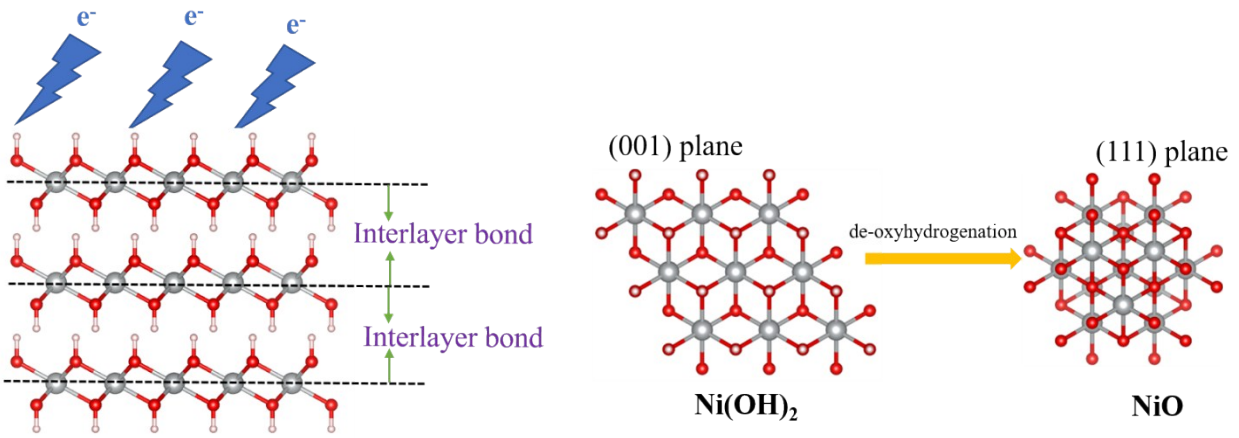

Fig. S15. Partial de-oxyhydrogenation process under low-dose TEM (white: H; red: O; grey: Ni). Under the low-dose TEM electron beam, the layered structure is retained due to the strong interlayer bond. With increasing dose, the de-oxyhydrogenation process occurs within the (001) plane, resulting in the formation of a NiO (111) plane. The sample is more beam-sensitive when the electron beam is perpendicular to the plane and decomposes to NiO, while it is less beam-sensitive if the electron beam is parallel with the layers.

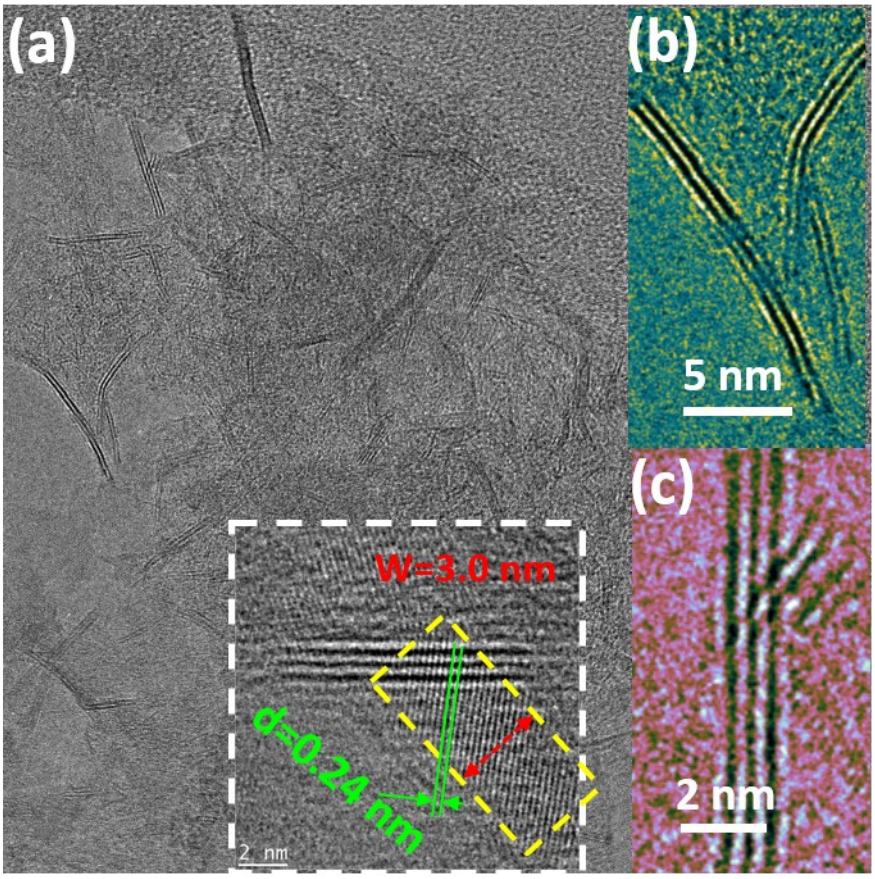

Fig. S16. Low-dose TEM images. (a) Low-dose TEM image showing double and triple layers, with enlarged image inset showing the plan-view structure. (b, c) Enlarged images focusing on one double and triple layer, respectively. The structure was further confirmed using low-dose TEM with a direct-detection camera. The results show similar information, double and triple $Ni(OH)_2$ layers, as shown in Figs. 16(a-c), which is consistent with our low-dose STEM observations. Furthermore, ribbon structures with widths of 2-5 nm and lengths of 10-20 nm are also observed, as shown in the inset of Fig. S16(a).

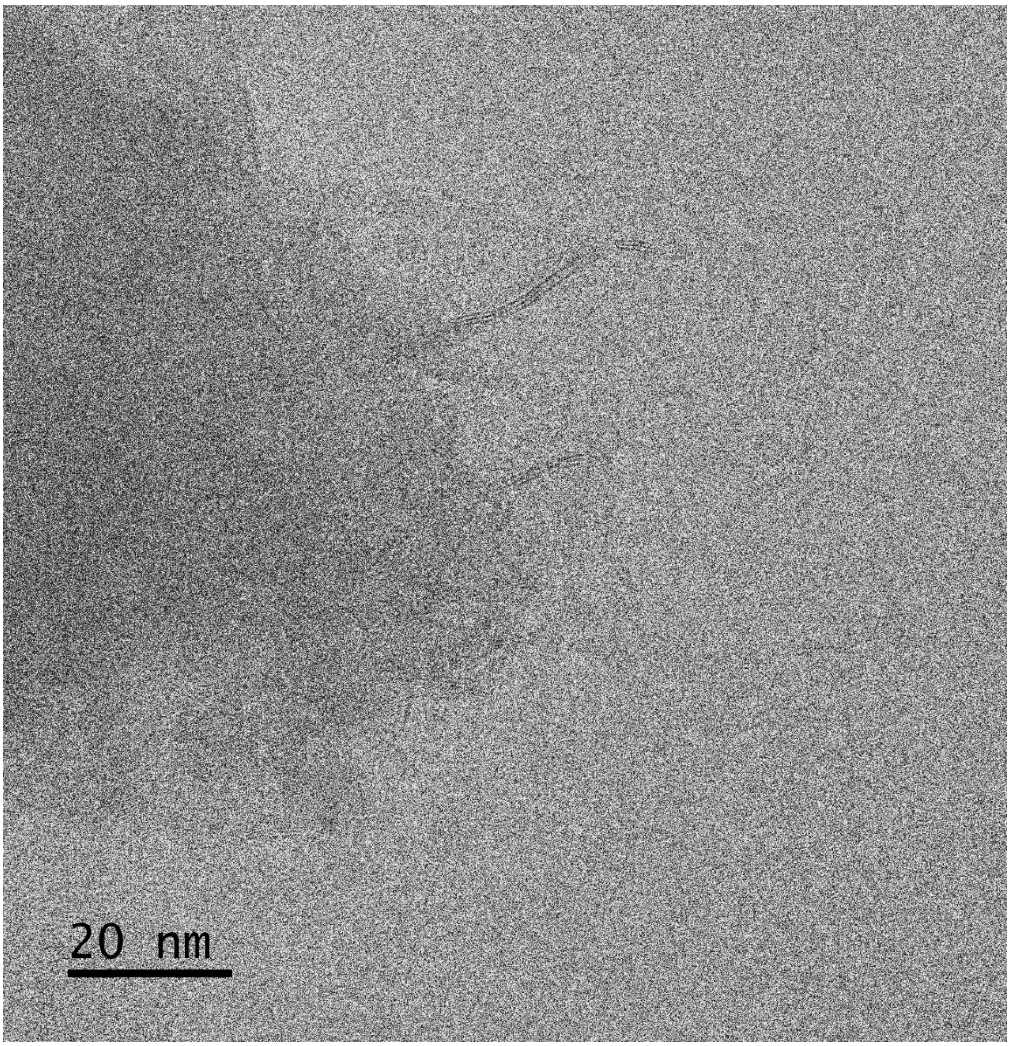

Fig. S17. L**ow-dose TEM images obtained with a cooling stage.** The triple-layer structure can be seen clearly. The accumulated electron dose in the image is ~90 electrons per $Å^2$ (1 second acquisition).

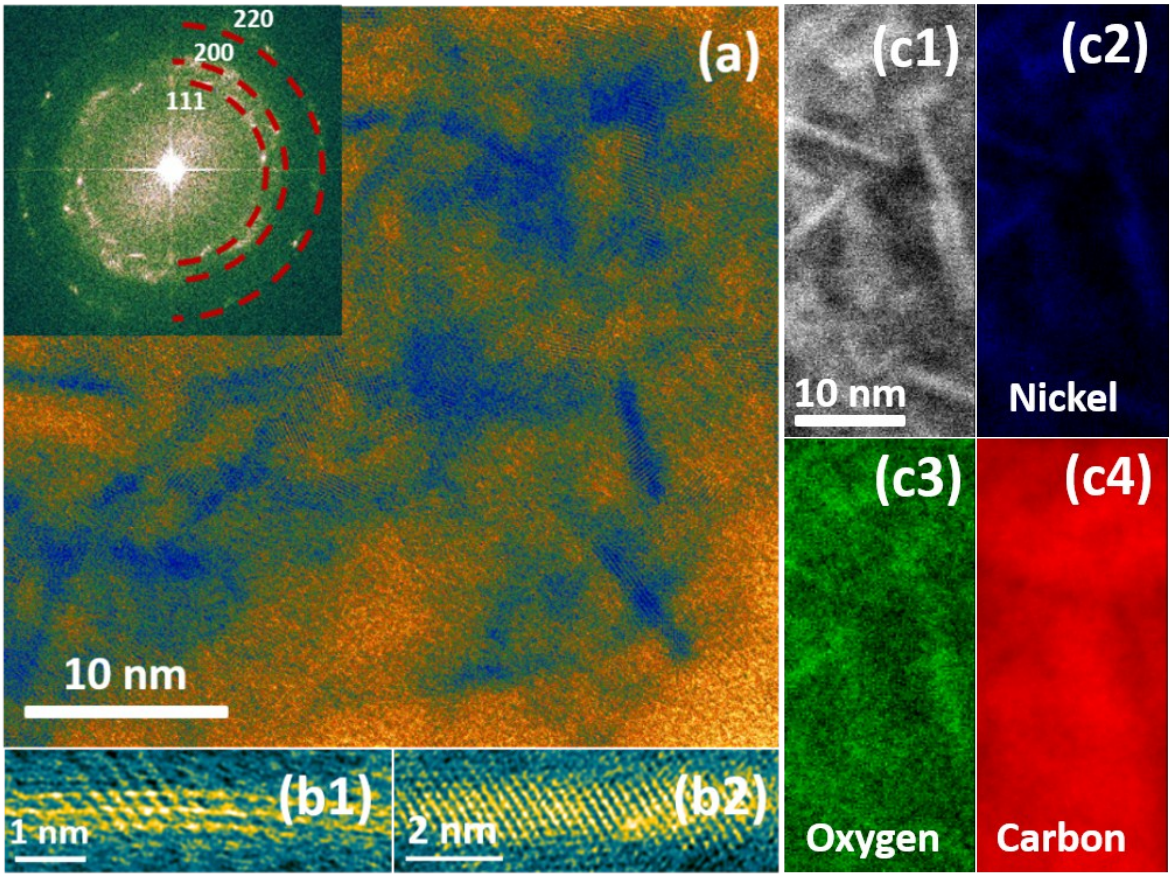

Fig. S18. STEM-EELS analysis. (a) Atomically-resolved STEM annular bright field (ABF) image showing nanorods, with its FFT image inset. (b1, b2) Enlarged images focusing on one nanorod along different orientations. Due to the high required dose for STEM-EDS/EELS composition analysis (with a large probe size, higher current density), the nanoribbons were decomposed into rod-like nanostructures with diameter of 2-3 nm and length of 10-20 nm. (c1-c4) STEM-EELS spectrum images with sub-nanometer resolution also show that the nanorods consist of Ni and O only, confirming that they are Ni-O compounds.

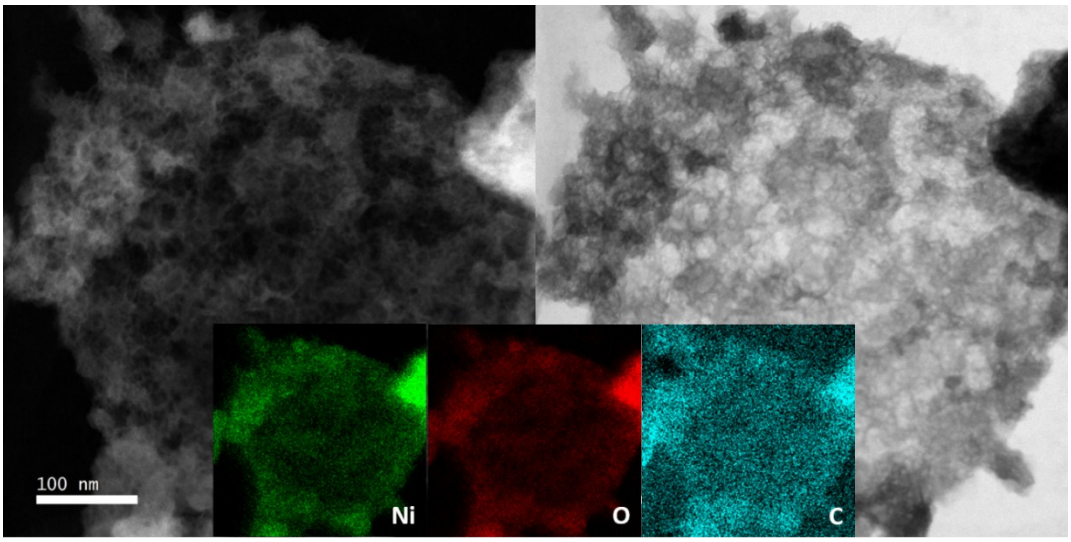

Fig. S19. Low-magnification STEM-HAADF (left) and ABF (right) images of NR-Ni(OH)$_2$ with STEM-EDX maps inset. The EDX elemental maps show a uniform distribution of Ni and O over a wide area.

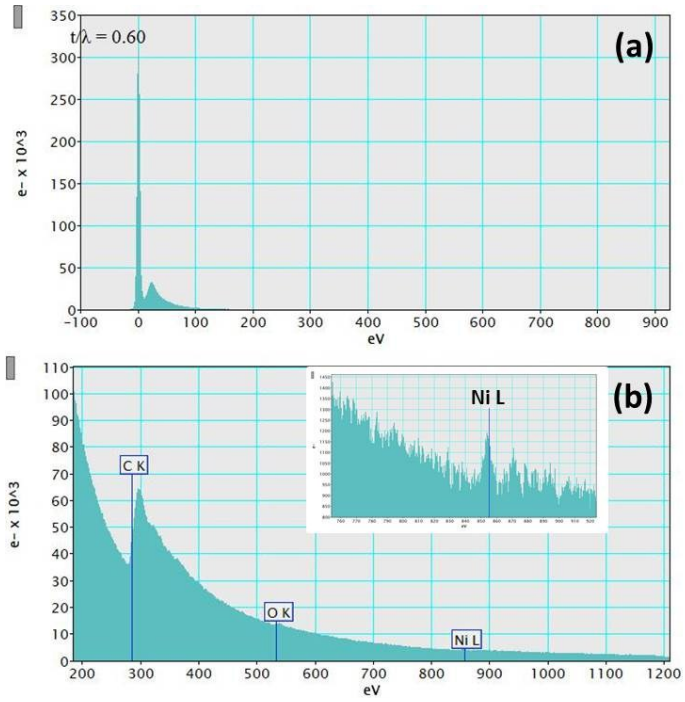

Fig. S20. Semi-quantitative EELS analysis of sample thickness and layer thickness. (a, b) Low-loss and high-loss EELS spectra obtained from one nanostructure, with an enlarged image inset for the Ni L edge.

	t/λ	t (nm)		C_com (at.%)	O_com (at.%)	Ni_com (at.%)	t_Ni (nm)
1	0.55	63		85	9.0	5.3	3.3
2	0.55	63		85	9.0	6.0	3.8
3	0.60	69		82	12	6.1	4.2
4	0.60	69		83	11	7.0	4.8
5	0.60	69		84	11	5.3	3.6
6	0.55	63		85	10	4.6	2.9
7	0.58	67		96	14	5.2	3.4
8	0.55	63		79	17	4.7	3.0
9	0.61	70		76	17	7.1	5.0
10	0.60	69		76	17	6.6	4.5
11	0.60	69		94	2.1	3.8	2.6
12	0.66	75		80	15	5.3	4.0
13	0.60	69		98	14	5.7	3.9
14	0.57	65		81	16	3.5	2.3
15	0.60	69		68	25	7.2	4.9
16	0.57	65		80	14	6.8	4.4
17	0.63	72		85	11	3.9	2.8
18	0.60	69		67	26	6.7	4.6
19	0.56	64		79	13	7.5	4.8
20	0.59	68		89	6.6	4.5	3.0
Average		67					3.8

Fig. S21. Semi-quantitative EELS analysis of sample thickness and nanoribbon width from different nanostructures. t/λ is obtained using the EELS log-ratio technique for specimen-thickness measurement (*9*), where t is the thickness and λ is the inelastic mean free path of electrons, which depends on materials and measurement conditions. Using the relative composition from EELS (labelled com) and the thickness, the approximate thickness of the nano ribbon can be estimated.

Summary of Figs S20 &21: The sample thickness varies from 60-75 nm, which includes the nanoribbons and the thick amorphous carbon matrix (*9*). Due to the thickness of the carbon, most nanoribbons are only visible edge-on. Through EELS composition analysis, the concentration of Ni lies in the range of 3.5-7.5 at.%, giving a thickness of 2-5 nm. Since these nanoribbons are measured edge-on, this figure corresponds to the width of the nanoribbons. In very thin areas of carbon some faint images can be seen corresponding to plan view images of decomposed nanoribbons. The widths of the decomposed nanoribbons are consistent with the above estimate.

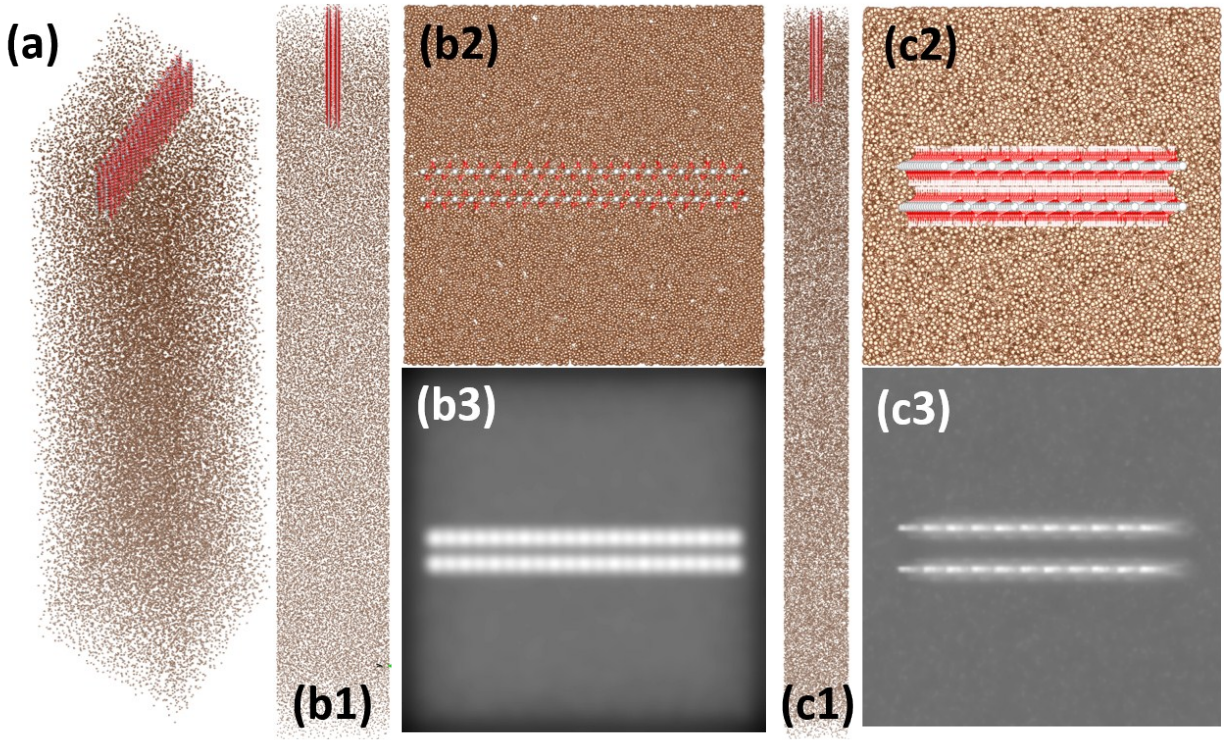

Fig. S22. Simulated STEM image. (a) Simulated structure model of one double-layer NR-$Ni(OH)_2$ (length: ~5.5 nm; width: ~4.1 nm) embedded within the carbon matrix (thickness: 50 nm). (b1-b3) Simulated image of one double-layer NR-$Ni(OH)_2$ (length: ~5.5 nm; width: ~4.1 nm) embedded in the surface of the carbon matrix (thickness: 50 nm). (c1-c3) Simulated image of the double-layer in a 60 nm carbon matrix, with the nanoribbon tilted 5^o away from the zone axis. (b1, c1) Views of layers from the side, along [100]. (b2, c2) Views of layers from the top, along [010]. (b3, c3) Simulated STEM HAADF images.

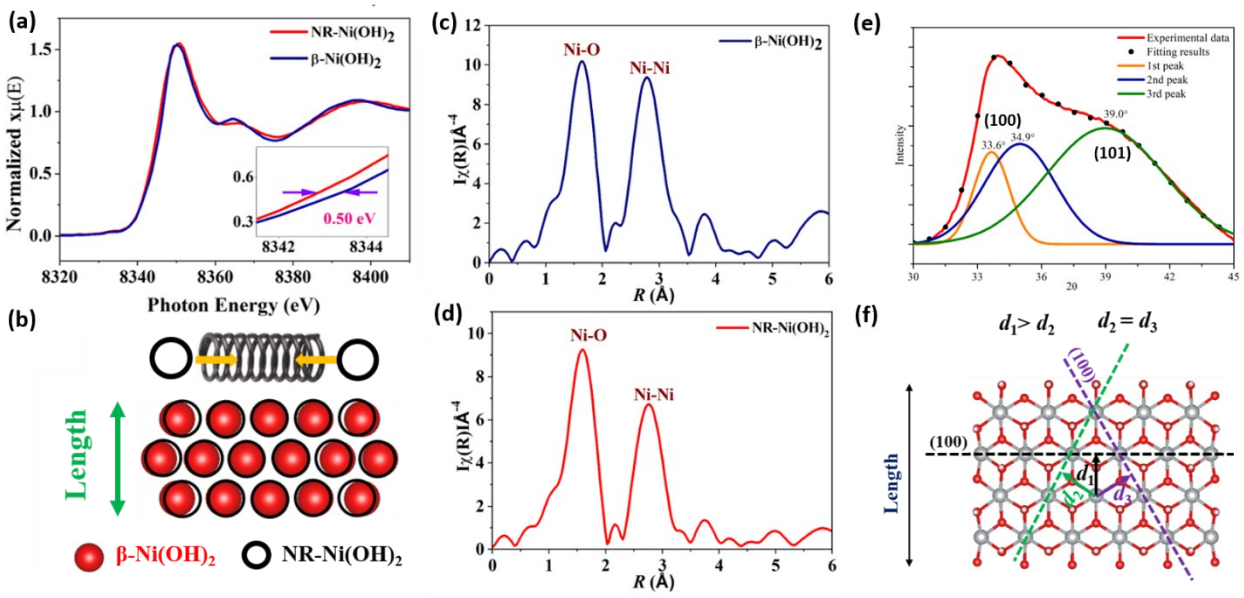

Fig. S23. (a) Ni *K* edge XANES spectra; (b) the model-matching method of NR-Ni(OH)$_2$ and β-Ni(OH)$_2$; (c) (d) The Fourier transform (FT) data of EXAFS analysis of NR-Ni(OH)$_2$ structure Ni; (e) SR-XRD fitting results in the angular range of 30-44° using Matlab Curve Fitting Toolbox; (f) The calculation model for (100) planar spacing in NR-Ni(OH)$_2$. The Ni(OH)$_2$ sample was examined using Ni *K*-edge X-ray absorption fine structure (XAFS), being benchmarked against conventional β-Ni(OH)$_2$. a, c and d show X-ray absorption near edge structure (XANES) analysis and FT data of the EXAFS. The XANES and FT data are quite close to those of β-Ni(OH)$_2$, implying they have very similar local chemical environment. However, some mismatch exists between the sample and β-Ni(OH)$_2$: The absorption edge of the sample is red shifted by ~0.50 eV (Inset of Fig. S23a) and its Ni-O bond length is around 0.03 Å shorter (Fig. S23 c and d) as compared to β-Ni(OH)$_2$ (More detailed structure information are shown in Table S1). The red shift in the adsorption edge indicates, the Ni in NR-Ni(OH)$_2$ has a lower average valence than that in β-Ni(OH)$_2$, which is lower than two. This is in accord well with DFT simulation model, that the armchair edges in NR-Ni(OH)$_2$ are fully consisted of periodically unsaturated Ni, which would result in the decrease of average Ni valence (Fig. 1m). The DFT simulation was used to study the lattice contraction within NR-Ni(OH)$_2$. Comparing with the relaxed β-Ni(OH)$_2$ model, the NR-Ni(OH)$_2$ shows that the obvious lattice contraction exists in the width direction especially at the edge, while only little contraction could be seen along the length direction. The oriented lattice contraction was further identified by the results of SR-XRD. As

shown in e and f, the (100) XRD peak is split, which suggests that the (100) plane spacing d_1 along the nanoribbon length direction is slightly larger than the other two equivalent plane spacings d_2 and d_3, as shown in the relaxed NR-$Ni(OH)_2$ structure. Combining XAFS, DFT calculations and SR-XRD, we could conclude that there is a tensile strain along the length direction in NR-$Ni(OH)_2$, which stabilize the four-coordinated Ni in NR-$Ni(OH)_2$.

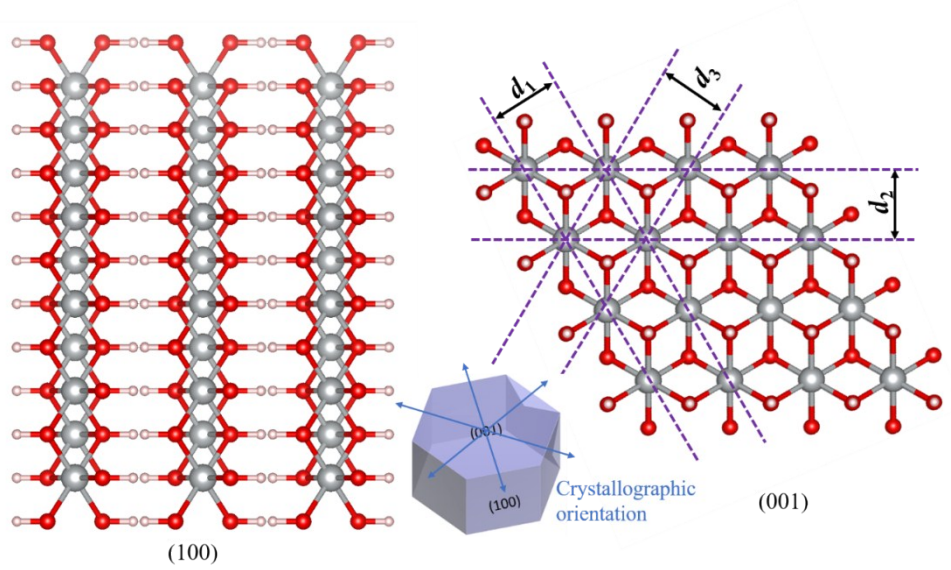

Fig. S24. The calculation model for (100) planar spacing. β-$Ni(OH)_2$ has six (100) equivalent planes and three equivalent (100) planar spacing d_1, d_2 and d_3, with six equivalent orientations, and prefers a disk-shape. For conventional β-$Ni(OH)_2$ with 2D planar stacking, d_1, d_2 and d_3 are the same. Thus, only one (100) diffraction peak can be seen. However, for our sample, the (100) diffraction peak is split into two peaks, suggesting that the (100) planar spacings d_1, d_2 and d_3 are no longer the same. This implies structural distortion exists in the (001) plane of the sample.

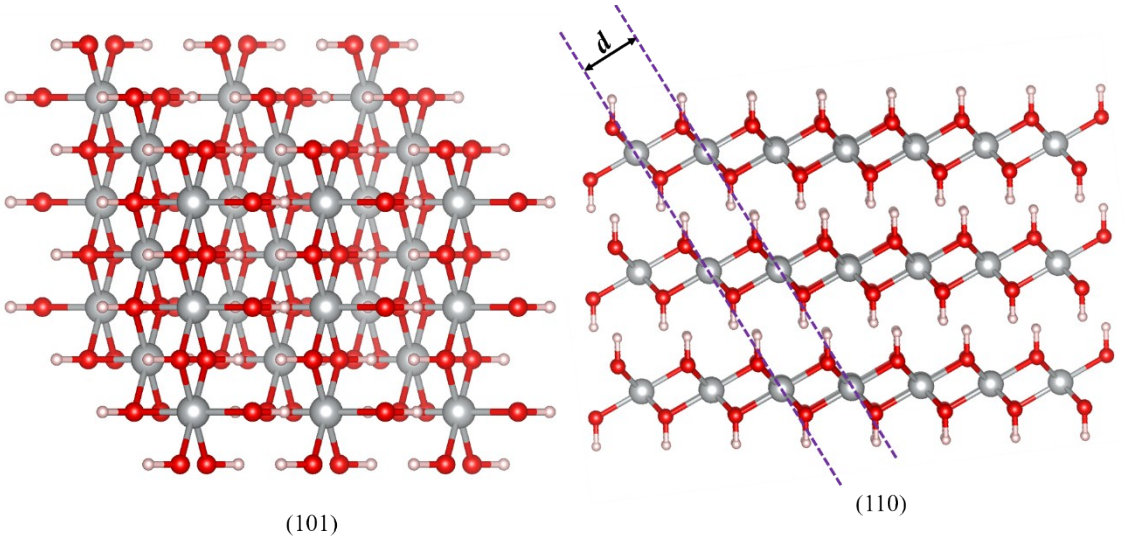

Fig. S25. Calculation model for the (101) plane and its corresponding (101) planar spacing *d*. The appearance of the (101) plane index suggested that the sample comprises a few layers instead of a single layer.

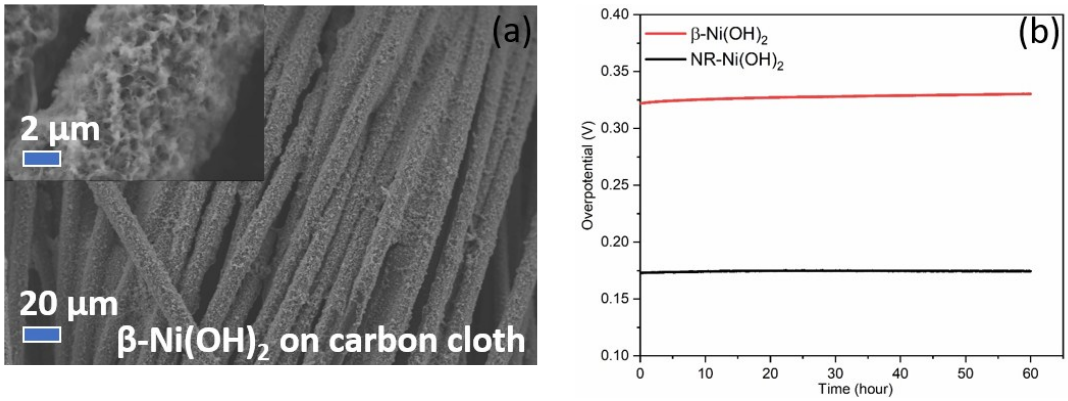

Fig. S26. **The morphology (a) and stability (b) of β-Ni(OH)$_2$.** It was observed that this sample had a porous structure which was uniformly grown on the carbon cloth. In the 60 hours' operation, the overpotential of NR-Ni(OH)$_2$ at 10 mA cm^{-2} was increased slightly from 0.173 V to 0.175 V. But the overpotential was increased from 0.32 V to 0.33 V for β-Ni(OH)$_2$. This clearly indicated that NR-Ni(OH)$_2$ had much better stability than β-Ni(OH)$_2$.

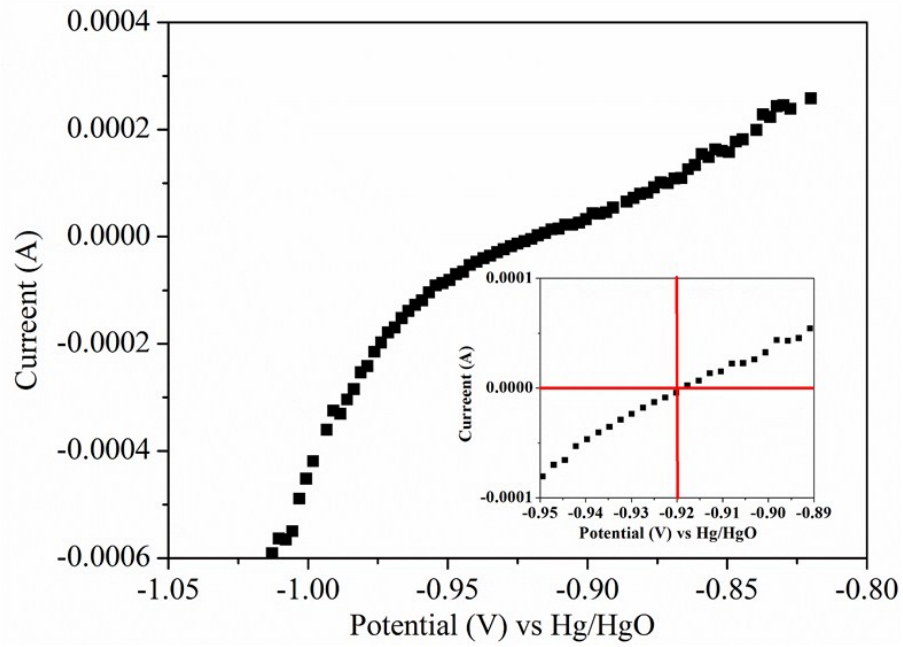

Fig. S27. **Linear scanning voltammetric curves.** It is measured in 1 M KOH aqueous electrolyte bubbled with Grade 4 H_2 gas using a three-electrode configuration, with the scan rate of 0.5 mV s^{-1} at room temperature (*7*).

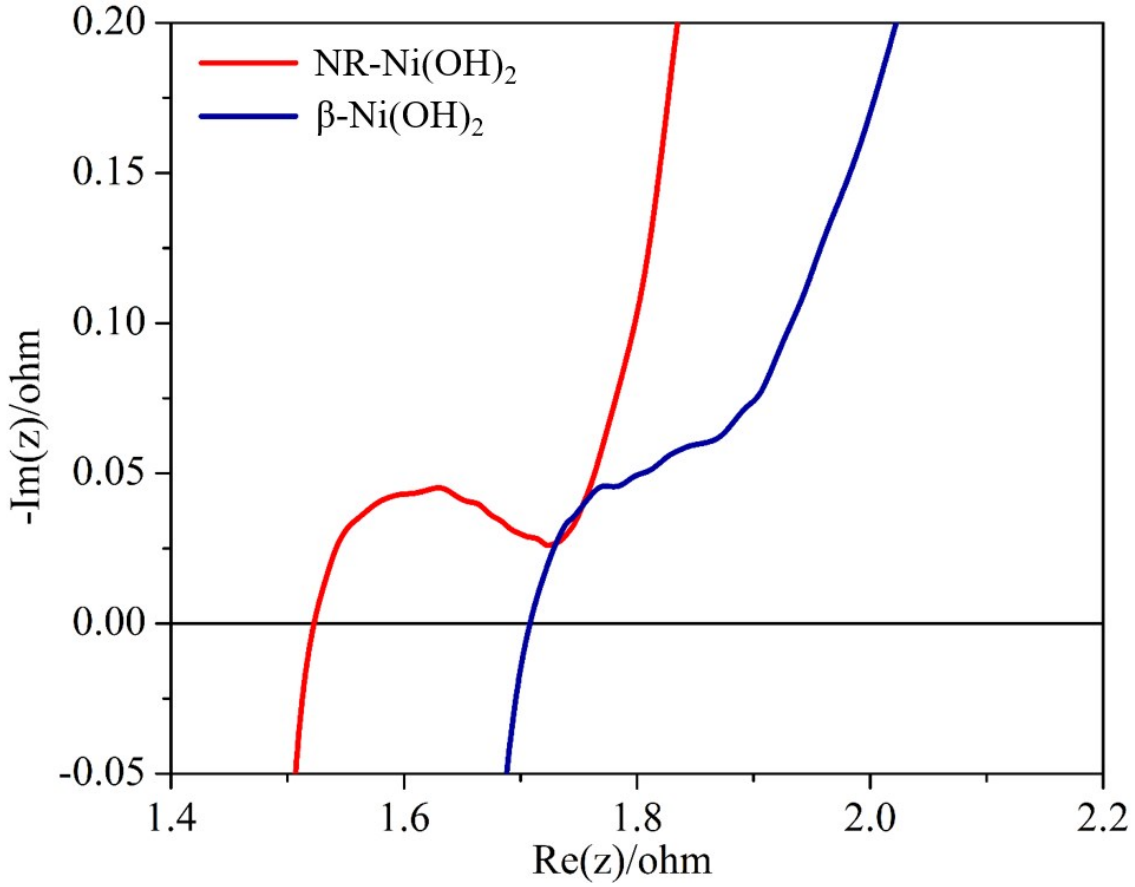

Fig. S28. **Electrochemical impedance spectroscopy data for NR-Ni(OH)$_2$ and the conventional β-Ni(OH)$_2$**. It is measured through three-electrode configuration in 1M KOH aqueous electrolyte. Through circle fitting, the resistances of NR-Ni(OH)$_2$ and conventional β-Ni(OH)$_2$ are 1.76 ohm and 1.84 ohm, respectively.

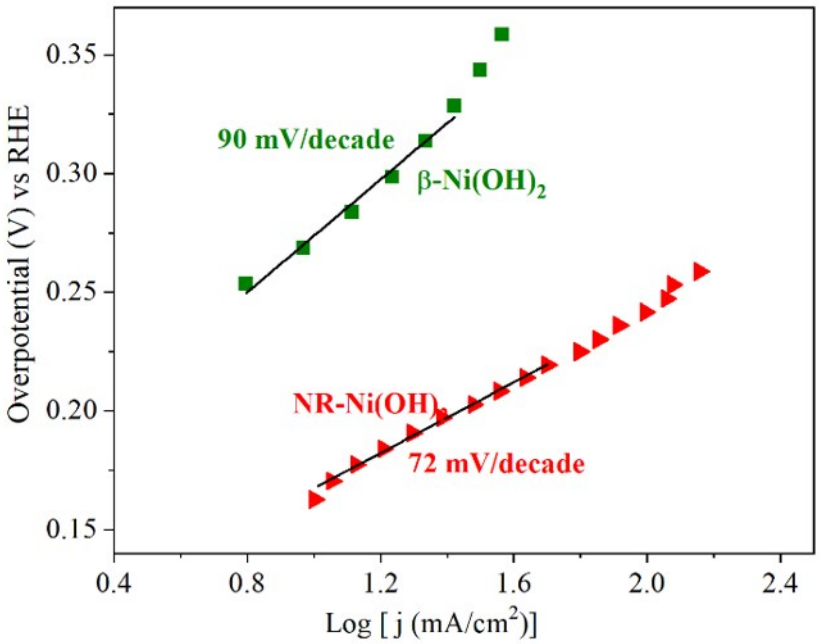

Fig. S29. **Tafel slopes based on current density normalized to the geometric area of NR-$Ni(OH)_2$ and conventional β-$Ni(OH)_2$.** When current is normalized to the geometric area, the corresponding Tafel slope of the NR-$Ni(OH)_2$ is 72 mV dec^{-1}, lower than that of β-$Ni(OH)_2$ (90 mV dec^{-1}).

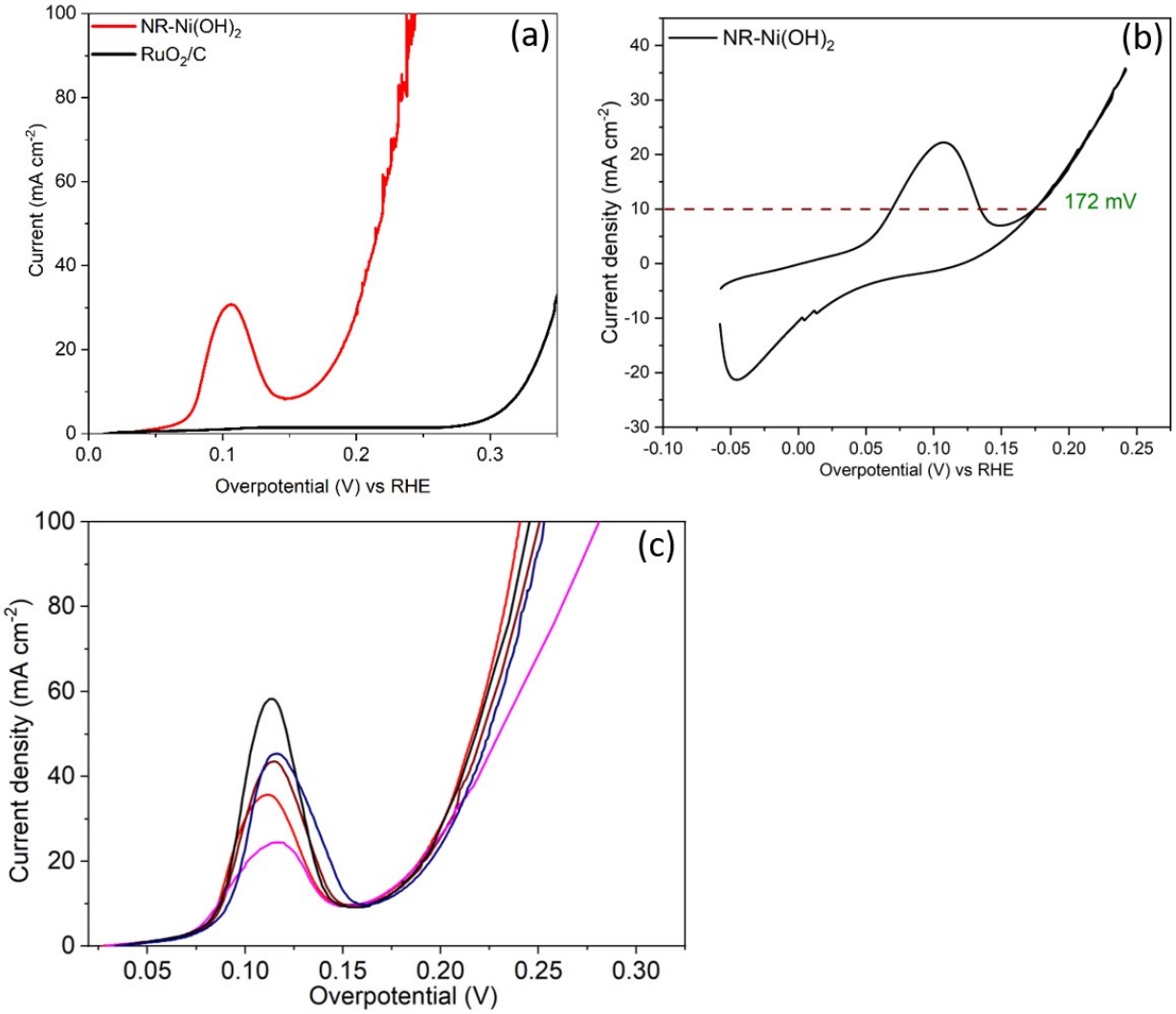

Fig. S30. (a) The OER comparison of NR-Ni(OH)$_2$ and RuO$_2$/C; (b) The CV measurement of NR-Ni(OH)$_2$; (c) The OER polarization curves of five other samples, with 0.1 mV s^{-1} scan rate and 90% *iR* correction. RuO$_2$/C required an overpotential of 315 mV to reach 10 mA cm^{-2}, which cannot be comparable to the NR-Ni(OH)$_2$. In the CV measurement it could be seen that the overpotential at 10 mA cm^{-2} was 172 mV in both the positive and negative scans. By considering the (1.1 ohm) ohmic compensation, the overpotential value is around 161 mV, which is nearly the same as that of the LSV measurement. The overpotentials of NR-Ni(OH)$_2$ at 10 mA cm^{-2} range from 158 mV to 165 mV.

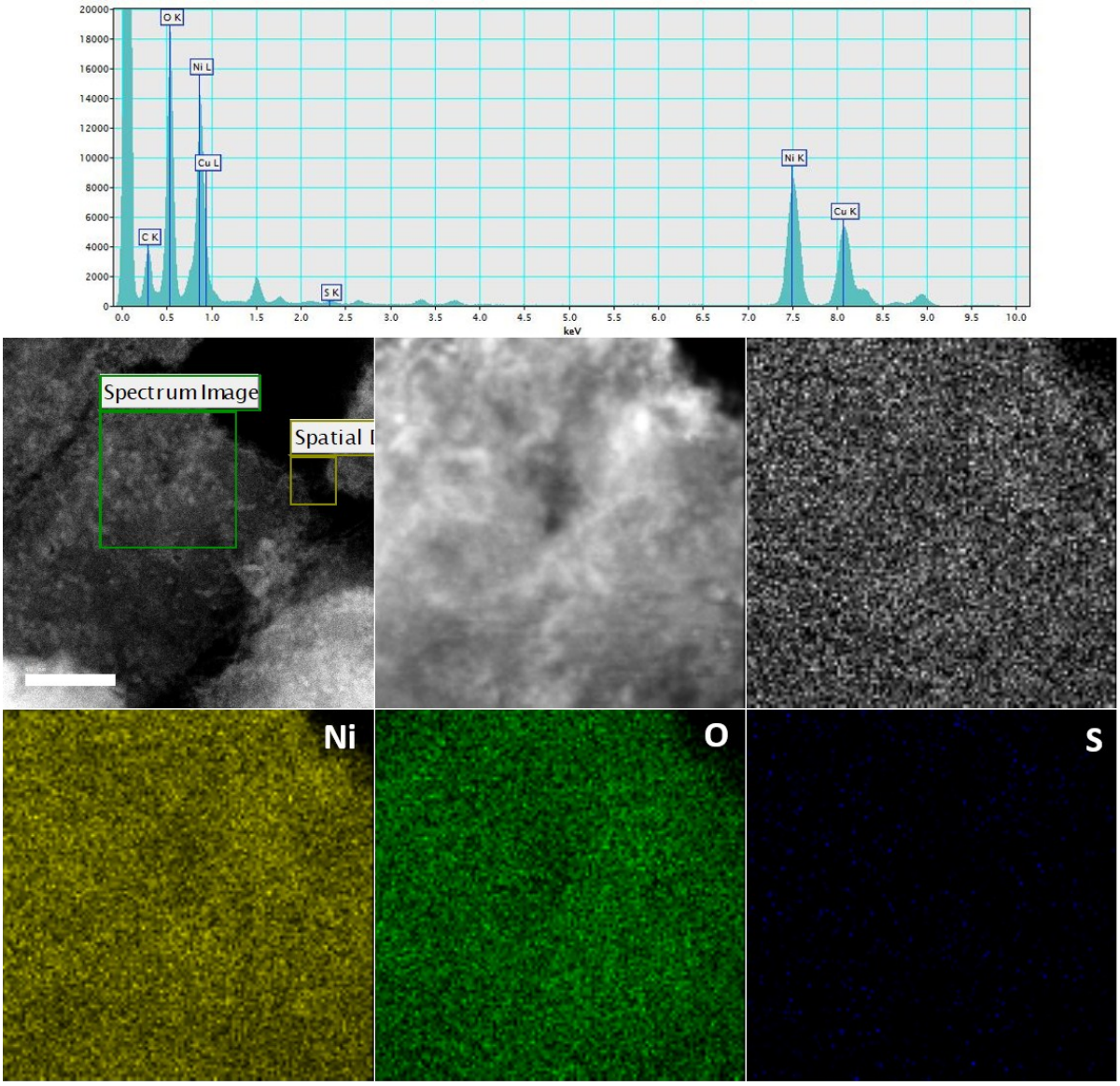

Fig. S31. STEM-EDS elemental mapping of after OER sample. Only Ni and O can be detected. Very little S signal could be found in the sample.

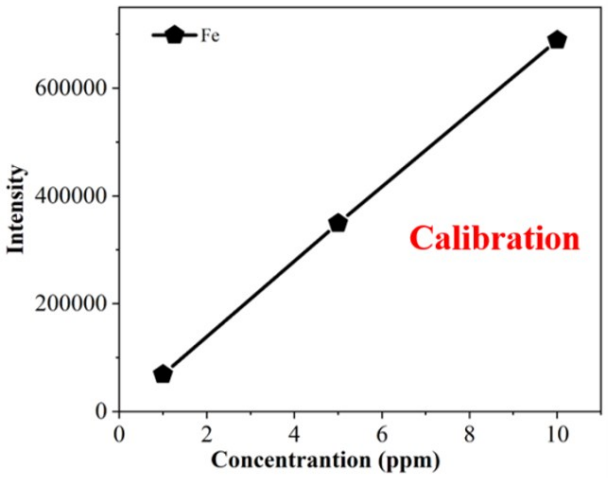

	Intensity	Concentration (ppm)
Blank	3762.0	0.054
Sample	5263.2	0.076

Fe content (wt%)	0.003

NR-Ni(OH)$_2$

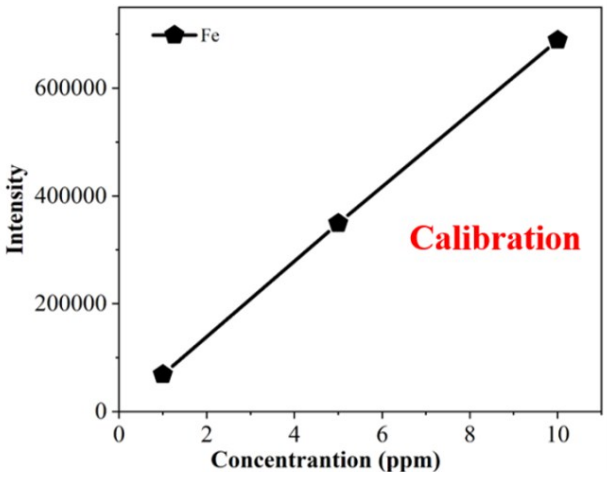

	Intensity	Concentration (ppm)
Blank	3692	0.053
Sample	699,390	10.04

Fe content (wt%)	2.000

β-Ni(OH)$_2$

Fig. S32. ICP analysis of Fe in the after OER sample. It has been well recognized that $Ni(OH)_2$ may incidentally take up Fe ion from ubiquitous sources in aqueous KOH under anodic potential. To confirm whether Fe was present in the obtained NR-$Ni(OH)_2$ samples, ICP chemical analysis was used. The sample was dissolved by a mixture of HNO_3 and HCl acids (1:3) on a hotplate and topped up to 10ml with H_2O. Standard Fe samples of 1 ppm, 5 ppm and 10 ppm were used for calibration. Blank and the sample were measured with the intensity value of 3762.0 and 5263.2 respectively. By calibration, for the blank the Fe concentration was 0.054 ppm and for sample it was 0.076 ppm. Taking the sample weight 6.3233 mg, the Fe content in the NR-$Ni(OH)_2$ sample was 0.003%. Through the same method, the Fe content in β-Ni(OH)2 is about 2.0%.

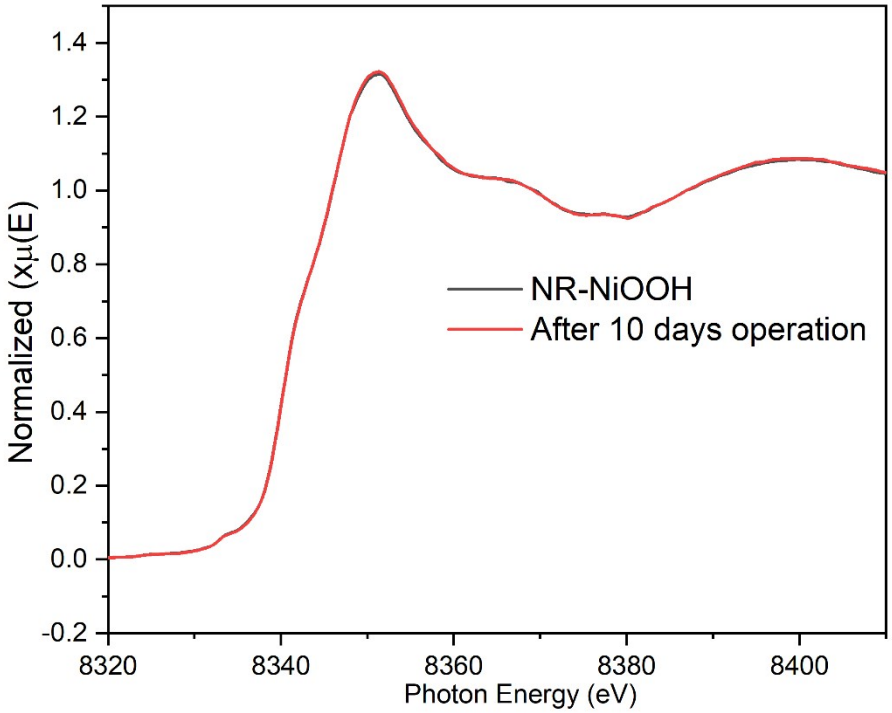

Fig. S33. The Ni *K*-edge XANES of NR-NiOOH and after 10 days operation. It is observed that these two curves are overlapped almost completely, which indicated that there is no obvious change in structure of the NR-NiOOH sample after 10 days of operation.

Table S1: EXAFS fitting results of β-$Ni(OH)_2$, NR-$Ni(OH)_2$, NR-NiOOH and NiS_2, where CN is the coordination number, R is the bond length and σ^2 is the Debye-Waller factor.

Samples	Bond species	CN	R (Å)	σ^2 (Å^2)	R factor
β-$Ni(OH)_2$	Ni-O	6.0*	2.07±0.01	0.0057±0.0006	0.0045
NR-$Ni(OH)_2$	Ni-O	6.4±0.6	2.04±0.01	0.0066±0.0007	0.0020
NR-NiOOH	Ni-O	5.1±0.5	1.85±0.01	0.0056±0.0006	0.0050
NiS_2	Ni-S	6.0*	2.41±0.01	0.0061±0.0006	0.0048

*Parameter fixed

Table S2: OER catalytic performance comparison between NR-$Ni(OH)_2$ and previously reported metal chalcogenides (sulfides and selenides) and pnictides (nitrides and phosphides)

Catalyst	Electrolyte	Overpotential (mV) at 10 mA cm^{-2} (Normalized to the geometric projected area)	Substrate	Ref
$Fe_{0.1}NiS_2$ NA/Ti	1M KOH	205	Ti foil	*9*
$Ni_{2.3\%}CoS_2$/C C	1M KOH	297	Carbon Cloth	*10*
CP/CTs/Co-S	1M KOH	306	Carbon Paper	*11*
$Zn_{0.76}Co_{0.24}S$/ CoS	1M KOH	300	Ti mesh	*12*
$Ni_{0.33}Co_{0.67}S_2$ nanowires	1M KOH	310	Ti foil	*13*
NiS nanosheet	1M KOH	297	Stainless Steel	*14*
CoS	1M KOH	361	Ti mesh	*15*
$CoNiS_8$ Octahedral nanocages	1M KOH	362	Glassy Carbon	*16*
A-$CoS_{4.6}O_{0.6}$ PNCs	1M KOH	290	Glassy Carbon	*17*
$CoSe_{0.85}$	1M KOH	324	Carbon Cloth	*18*
$(Ni,Co)Se_{0.85}$	1M KOH	255	Carbon Cloth	*18*
$(Ni,Co)Se_{0.85}$-NiCo LDH	1M KOH	216	Carbon Cloth	*18*
$NiSe_2$-DO	1M KOH	241	Nickel foam	*19*
$Ni_xFe_{1-x}Se_2$-DO	1M KOH	195	Nickel foam	*19*
Co_3N	1M KOH	410	Glassy Carbon	*20*
Co_4N	1M KOH	330	Glassy Carbon	*20*
Co_4N	1M KOH	257	Carbon Cloth	*21*
Ni_3N	1M KOH	490	Carbon Cloth	*22*
Ni_3N nanosheet	1M KOH	350	Glassy Carbon	*22*
Ni_3FeN	1M KOH	223	Nickel foam	*23*
Ni_3N COF	1M KOH	230	Glassy Carbon	*24*
Ni_2P	1M KOH	290	Nickel foam	*25*
Ni_2P/Ni/NF	1M KOH	205	Nickel	*25*

			foam	
Ni_2P/NF	1M KOH	220	Nickel foam	*25*
Co_2P NPs	1M KOH	310	Copper foil	*22*
CoP/Ti mesh	1M KOH	310	Ti mesh	*26*
Ni_5P_4	1M KOH	330	Nickel foil	*27*
Mn-Co oxyphosphide	1M KOH	320	Glassy Carbon	*28*
NiFeP	1M KOH	219	Glassy carbon	*29*
$Ni_{1.25}Ru_{0.75}P$	1M KOH	340	Glassy carbon	*30*
NiCoP nano box	1M KOH	330	Glassy carbon	*31*
CoNi(20:1)-P-NS@NF	1M KOH	209	Nickel foam	*32*
$(Ni_{0.5}Fe_{0.5})_2P$ microflower	1M KOH	203	Nickel foam	*33*
Co_3O_4@CoP	1M KOH	238	Nickel foil	*34*
NR-Ni(OH)$_2$	**1M KOH**	**162**	**Carbon cloth**	**Our work**
NR-Ni(OH)$_2$	**1M KOH**	**210**	**Glassy carbon**	**Our work**

Table S3: OER catalytic performance comparison between NR-$Ni(OH)_2$ and previously reported metal oxide/hydroxide/oxyhydroxide.

Catalyst	Electrolytes	Overpotential (mV) at 10 mA cm^{-2} (Normalized to the geometric projected area)	Substrate	Ref
(Ni,Fe,Ti,La)OH	1M KOH	260	HOPG	*35*
(NiFe) LDH	0.1 M KOH	290	Glassy carbon	*36*
FeNi-rGO LDH	1 M KOH	206	Nickel foam	*37*
Single-layer NiFe LDH	1 M KOH	300	Glassy carbon	*38*
Co_3O_4/N-rmGO	1 M KOH	310	Glassy carbon	*39*
$NiFeO_x$ nano particle	1 M KOH	280	Carbon fiber paper	*40*
G-FeCoW	1 M KOH	223	Glassy carbon	*7*
G-FeCoW	1 M KOH	191	Gold-plated nickel foam	*7*
α-$Ni(OH)_2$	1 M KOH	331	Glassy carbon	*41*
$Na_{0.08}Ni_{0.9}Fe_{0.1}O_2$	1M KOH	260	Glassy carbon	*42*
$CoFe_2O_4$/C	1M KOH	240	Nickel foam	*43*
Fe_1Co_1-ONS	1M KOH	308	Glassy carbon	*44*
Ni_3Mn_1 LDH	1M KOH	350	Glassy carbon	*45*
$MnFe_2O_4$	0.1M KOH	470	Glassy carbon	*46*
$CoFe_2O_4$	0.1M KOH	370	Glassy carbon	*46*
$NiFe_2O_4$	0.1M KOH	440	Glassy carbon	*46*
$CuFe_2O_4$	0.1M KOH	410	Glassy carbon	*46*
NiCo oxide	1M KOH	340	FTO	*47*
CS-NiFeCu	1M KOH	180	Nickel foam	*62*
NR-$Ni(OH)_2$	**1 M KOH**	**162**	**Carbon cloth**	**Our work**
NR-$Ni(OH)_2$	**1M KOH**	**210**	**Glassy carbon**	**Our work**

Table S4: OER catalytic performance comparison between NR-$Ni(OH)_2$ and previously reported novel metal based (56-59), perovskite (60-63), MOF based materials (64-66), and carbon materials (67-68).

Catalyst	Electrolytes	Overpotential (mV) at 10 mA cm^{-2} (Normalized to the geometric projected area)	Substrate	Ref
(Ni,Fe,Ti,La)OH	1M KOH	260	HOPG	*35*
(NiFe) LDH	0.1 M KOH	290	Glassy carbon	*36*
FeNi-rGO LDH	1 M KOH	206	Nickel foam	*37*
Single-layer NiFe LDH	1 M KOH	300	Glassy carbon	*38*
Co_3O_4/N-rmGO	1 M KOH	310	Glassy carbon	*39*
$NiFeO_x$ nano particle	1 M KOH	280	Carbon fiber paper	*40*
G-FeCoW	1 M KOH	223	Glassy carbon	*7*
G-FeCoW	1 M KOH	191	Gold foam	*7*
α-$Ni(OH)_2$	1 M KOH	331	Glassy carbon	*41*
$Na_{0.08}Ni_{0.9}Fe_{0.1}O_2$	1M KOH	260	Glassy carbon	*42*
$CoFe_2O_4$/C	1M KOH	240	Nickel foam	*43*
Fe_1Co_1-ONS	1M KOH	308	Glassy carbon	*44*
Ni_3Mn_1 LDH	1M KOH	350	Glassy carbon	*45*
$MnFe_2O_4$	0.1M KOH	470	Glassy carbon	*46*
$CoFe_2O_4$	0.1M KOH	370	Glassy carbon	*46*
$NiFe_2O_4$	0.1M KOH	440	Glassy carbon	*46*
$CuFe_2O_4$	0.1M KOH	410	Glassy carbon	*46*
NiCo oxide	1M KOH	340	FTO	*47*
CS-NiFeCu	1M KOH	180	Nickel foam	*62*
NR-$Ni(OH)_2$	**1 M KOH**	**162**	**Carbon cloth**	**Our work**
NR-$Ni(OH)_2$	**1M KOH**	**210**	**Glassy carbon**	**Our work**

Table S5. The calculated reaction energy of β-NiOOH (*63*).

Reaction step	Free energies (eV)	Overpotential (V)
$H_2O^* \rightarrow OH^* + (H^+ + e^-)$	0.75	-
$OH^* \rightarrow O^* + (H^+ + e^-)$	0.99	-
$O^* + H_2O \rightarrow OOH^* + (H^+ + e^-)$	1.79	0.62
$OOH^* \rightarrow O_2^* + (H^+ + e^-)$	1.27	-

Our calculation results

Reaction step	Free energies (eV)	Overpotential (V)
$H_2O \rightarrow OH^* + (H^+ + e^-)$	0.80	-
$OH^* \rightarrow O^* + (H^+ + e^-)$	1.00	-
$O^* + H_2O \rightarrow OOH^* + (H^+ + e^-)$	1.78	0.63
$OOH^* \rightarrow O_2 + (H^+ + e^-)$	1.02	-

Table S6. Corrections to the Gibbs free energies (in eV) for adsorbates in the gas phase and on the (110) surface. ZPE, vibrational enthalpies (H_{vib}) and entropy contributions to the Gibbs free energies are calculated at T=300 K and P=1 atm.

	ZPE	H_{vib}	TS	ZPE+H_{vib}+TS
H_2O	0.5564	0.104	0.67	-0.0096
H_2	0.2653	0.09	0.41	-0.0547
O*	0.119	0.03	0.08	0.069
OH*	0.345	0.046	0.08	0.311
OOH*	0.410	0.078	0.12	0.368

Reference List:

1. J. Perdew, K. Burke, M. Ernzerhof, Generalized Gradient Approximation Made Simple. *Phys. Rev. Lett.* **77,** 3865 (1996).

2. P. Blöchl, Projector augmented-wave method, *Phys. Rev. B* **50**, 17953 (1994).

3. G. Kresse, J. Furthmüller, Efficiency of ab-initio total energy calculations for metals and semiconductors using a plane-wave basis set, *Comput. Mater. Sci.* **16** 15 (1996).

4. I. C. Man, H.-Y. Su, F. Calle-Vallejo, H. A. Hansen, J. I. Martínez, N. G. Inoglu, J. Kitchin, T. F. Jaramillo, J. K. Nørskov, J. Rossmeisl, Universality in Oxygen Evolution Electrocatalysis on Oxide Surfaces. *ChemCatChem* 3, 1159–1165 (2011).

5. X. M. Cao, R. Burch, C. Hardacre, P. Hu, An understanding of chemoselective hydrogenation on crotonaldehyde over Pt(111) in the free energy landscape: The microkinetics study based on first-principles calculations, *Catalysis Today* 165, 71–79 (2011).

for Electrocatalytic Water Splitting, *J. Am. Chem. Soc.* 137, 1305−1313 (2015).

6. B. Ravel, M. Newville, Athena, Artemis, Hephaestus: data analysis for X-ray absorption spectroscopy using IFEFFIT. *J. Synchrotron. Rad.* **12,** 537 - 541 (2005).

7. B. Zhang, X. Zheng, O. Voznyy, R. Comin, M. Bajdich, M. Garcia-Melchor, L. Han, J. Xu, M. Liu, L. Zheng, F G. D. Arguer, G. T. Dinh, F. Fan, M. Yuan, E. Yassitepe, N. Chen, T. Regier, P. Liu, Y. Li, P. D. Luna, A. Janmohamed, H. L. Xin, H. Yang, A. Vojvodic, E. H. Sargent, Homogeneously dispersed multimetal oxygen-evolving catalysts. *Science* **352,** 333-337 (2016).

8. S. Yoshio, K. Maki, Computional modeling of the effect of varing aqueous solutional on $Ni(OH)_2$ precipitate. *AIP. Adv.* **8,** 025217 (2018).

9. A. E. Lewis, Review of metal sulphide precipitation. *Hydrometallurgy* **104,** 222-234 (2010).

10. W. Fang, D. Liu, Q. Lu, X. Sun, A. M. Asiri, Nickel promoted cobalt disulfide nanowire array supported on carbon cloth: An efficient and stable bifunctional electrocatalyst for full water splitting. *Electrochemistry Communications* **63,** 60-64 (2016).

11. J. Wang, H. Zhong, Z. Wang, F. Meng, X. Zhang, Integrated three-dimensional carbon paper/carbon tubes/cobalt-sulfide sheets as an efficient electrode for overall water splitting. *ACS nano* **10,** 2342-2348 (2016).

12. Y. Liang, Q. Liu, Y. Luo, X. Sun, Y. He, A. M. Asiri, $Zn_{0.76}Co_{0.24}S/CoS_2$ nanowires array for efficient electrochemical splitting of water. *Electrochimica Acta* **190,** 360-364 (2016).

13. Z. Peng, D. Jia, A. M. Al-Enizi, A. A. Elzatahry, G. Zheng, From water oxidation to reduction: homologous Ni-Co based nanowires as complementary water splitting electrocatalysts. *Adv. Energy Mater*. **5,** 1402031 (2015).

14. J. Chen, J. Ren, M. Shalom, T. Fellinger, M. Antonietti, Stainless steel mesh-supported NiS nanosheet array as highly efficient catalyst for oxygen evolution reaction. *ACS Appl, Mater. Interfaces* **2016,** 8, 5509-5516.

15. T. liu, Y. Liang, Q. Liu, X. Sun, Y. He, A. M. Asiri, Tingting, Electrodeposition of cobalt-sulfide nanosheets film as an efficient electrocatalyst for oxygen evolution reaction. *Electrochem. Commun.* **60,** 92-96 (2015).

16. J. Kim, H. Jin, A. Oh, H. Baik, S. H. Joo, K. Lee, Synthesis of compositionally tunable, hollow $Co_xNi_yS_z$ octahedral nanocages and their composition-dependent electrocatalytic activities for oxygen evolution reaction. *Nanoscale*, **9,** 15397 (2017).

17. P. Cai, J. Huang, J. Chen, Z. Wen, Oxygen-Containing Amorphous Cobalt Sulfide Porous Nanocubes as High-Activity Electrocatalysts for the Oxygen Evolution Reaction in an Alkaline/Neutral Medium. *Angew. Chem. Int. Ed.* **56,** 4858-4861.

18. C. Xia, Q. Jiang, C. Zhao, M. N. Hedhili, H. N. Alshareef, Selenide-Based Electrocatalysts and Scaffolds for Water Oxidation Applications. *Adv. Mater.* **28,** 77-85 (2016).

19. X. Xiang, F. Song, X. Hu, A nickel iron diselenide-derived efficient oxygen-evolution catalyst. *Nat. Commun.* **7,** 12324 (2016).

20. P. Chen, K. Xu, Y. Tong, X. Li, S. Tao, Z. Fang, W. Chu, X. Wu, C. Wu, Cobalt nitrides as a class of metallic electrocatalysts for the oxygen evolution reaction. *Inorg. Chem. Front.* **3,** 236-242 (2016).

21. P. Chen, K. Xu, Z. Fang, Y. Tong, J. Wu, X. Lu, X. Peng, H. Ding, C. Wu, Y. Xie, Metallic Co_4N porous nanowire arrays activated by surface oxidation as electrocatalysts for the oxygen evolution reaction. *Angew. Chem.* **127,** 14923-14927 (2015).

22. K. Xu, P. Chen, X. Li, Y. Tong, H. Ding, X. Wu, W. Chu, Z. Peng, C. Wu, Y. Xie, Metallic nickel nitride nanosheets realizing enhanced electrochemical water oxidation. *J. Am. Chem. Soc.* **137,** 4119-4125 (2015).

23. Y. Wang, C. Xie, D. liu, X. Huang, J. Huo, S. Wang, Nanoparticle-stacked Porous nickel–iron nitride nanosheet: a highly efficient bifunctional electrocatalyst for overall water splitting. *ACS Appl. Mater. Interfaces.* **8,** 18652-18657 (2016).

24. S. Nandi, S. K. Singh, D. Mullangi, R. Illathvalappil, L. George, C. P. Vinod, S. Kurungot, Low band gap benzimidazole COF supported Ni_3N as highly active OER catalyst. *Adv. Energy. Mater.* **6,** 1601189 (2016).

25. B. You, N. Jiang, M. Sheng, M. W. Bhushan, Y. Sun, Hierarchically porous urchin-like Ni_2P superstructures supported on nickel foam as efficient bifunctional electrocatalysts for overall water splitting. *ACS. Catal.* **6,** 714-721 (2016).

26. L. Yang, H. Qi, C. Zhang, X. Sun, An efficient bifunctional electrocatalyst for water splitting based on cobalt phosphide. Nanotechnology **27,** 23LT01 (2016).

27. M. Ledendecker, S. K. Calderón, C. Papp, H. Steinrück, M. Antonietti, M. Shalom, The synthesis of nanostructured Ni_5P_4 films and their use as a non-noble bifunctional electrocatalyst for full water splitting. *Angew. Chem.* **127,** 12538-12542 (2015).

28. B. Guan, L. Yu, X. Lou, General synthesis of multishell mixed-metal oxyphosphide particles with enhanced electrocatalytic activity in the oxygen evolution reaction. *Angew. Chem. Int. Ed.* **56,** 2386-2389 (2017).

29. F. Hu, S. Zhu, S. Chen, Y. Li, L. Ma, T. Wu, Y. Zhang, C. Wang, C. Liu, X. Yang, L. Song, X. Yang, Y. Xiong, Amorphous metallic NiFeP: a conductive bulk material achieving high activity for oxygen evolution reaction in both alkaline and acidic media. *Adv. Mater.* **29,** 1606570 (2017).

30. D. R. Liyanage, D. Li, Q. B. Cheek, H. Baydoun, S. L. Brock, Synthesis and oxygen evolution reaction (OER) catalytic performance of $Ni_{2-x}Ru_xP$ nanocrystals: enhancing activity by dilution of the noble metal. *J. Mater Chem. A.* **5,** 17609 (2017).

31. P. He, X. Yu, X. Lou, Carbon-incorporated nickel–cobalt mixed metal phosphide nanoboxes with enhanced electrocatalytic activity for oxygen evolution. *Angew. Chem.* **129,** 3955-3958(2017).

32. X. Xiao, C. He, S. Zhao, J. Li, W. Lin, Z. Yuan, Q. Zhang, S. Wang, L. Dai, D. Yu, A general approach to cobalt-based homobimetallic phosphide ultrathin nanosheets for highly efficient oxygen evolution in alkaline media. *Energy & Environ. Sci.* **10,** 893 (2017).

33. J. Yu, G. Cheng, W. Luo, Hierarchical NiFeP microflowers directly grown on Ni foam for efficient electrocatalytic oxygen evolution. *J. Mater. Chem. A.* **5,** 11229 (2017).

34. J. Zhou, Y. Dou, A. Zhou, R. Guo, M. Zhao, J. Li, MOF template-directed fabrication of hierarchically structured electrocatalysts for efficient oxygen evolution reaction. *Adv. Energy. Mater.* **7,** 1602643 (2017).

35. B. M. Hunter, J. D. Blakemore, M. Deimund, H. B. Gray, J. R. Winkler, A. M. Müller, Highly active mixed-metal nanosheet water oxidation catalysts made by pulsed-laser ablation in liquids. *J. Am. Chem. Soc.* **136,** 13118-13121 (2014).

36. M. Gong, Y. Li, H. Wang, Y. Liang, J. Z. Wu, J. Zhou, J. Wang, T. Reger, F. Wei, H. Dai, An advanced Ni–Fe layered double hydroxide electrocatalyst for water oxidation. *J. Am. Chem. Soc.* **135,** 8452-8455 (2013).

37. X. Long, J. Li, S. Xiao, K. Yan, Z. Wang, H. Chen, S. Yang, A strongly coupled graphene and FeNi double hydroxide hybrid as an excellent electrocatalyst for the oxygen evolution reaction. *Angew. Chem.* **126,** 7714-7718 (2014).

38. F. Song, X. Hu, Exfoliation of layered double hydroxides for enhanced oxygen evolution catalysis. *Nat. Commun.* **5,** 4477 (2014).

39. Y. Liang, Y. Li, H. Wang, J. Zhou, J. Wang, T. Regier, H. Dai, Co_3O_4 nanocrystals on graphene as a synergistic catalyst for Oxygen Reduction Reaction. *Nat. Mater.* **10,** 780-786 (2011).

40. H. Wang, H. Lee, Y. Deng, Z. Lu, P. Hsu, Y. Liu, D. Lin, Y. Cui, Bifunctional non-noble metal oxide nanoparticle electrocatalysts through lithium-induced conversion for overall water splitting. *Nat. Commun.* **6,** 7261(2015).

41. M. Gao, W. Sheng, Z. Zhuang, Q. Fang, S. Gu, J. Jiang, Y. Yan, Efficient water oxidation using nanostructured α-nickel-hydroxide as an electrocatalyst. *J. Am. Chem. Soc.* **136,** 7077-7084 (2014).

42. B. Weng, F. Xu, C. Wang, W. Meng, C. R. Grice, Y. Yan, A layered $Na_{1-x}Ni_yFe_{1-y}O_2$ double oxide oxygen evolution reaction electrocatalyst for highly efficient water-splitting. *Energy. Environ. Sci.* **10,** 121-128 (2017).

43. X. Lu, L. Gu, J. Wang, J. Wu, P. Liao, G. Li, Bimetal-organic framework derived $CoFe_2O_4$/C porous hybrid nanorod arrays as high-performance electrocatalysts for oxygen evolution reaction. *Adv. Mater.* **29,** 1604437 (2017).

44. L. Zhuang, L. Ge, Y. Yang, M. Li, Y. Jia, X. Yao, Z. Zhu, Ultrathin iron-cobalt oxide nanosheets with abundant oxygen vacancies for the oxygen evolution reaction. *Adv. Mater.* **29,** 1606793 (2017).

45. A. Sumbja, J. Chen, Y. Zong, P. S. Lee, Z. Liu, NiMn layered double hydroxides as efficient electrocatalysts for the oxygen evolution reaction and their application in rechargeable Zn–air batteries. *Nanoscale* **9,** 774 (2017).

46. M. Li, Y. Xiong, X. Liu, X. Bo, Y. Zhang, C. Han, L. Guo, Facile synthesis of electrospun MFe_2O_4 (M= Co, Ni, Cu, Mn) spinel nanofibers with excellent electrocatalytic properties for oxygen evolution and hydrogen peroxide reduction. *Nanoscale* **7,** 8920 (2015).

47. H. Wang, Y. Hsu, R. Chen, T. Chan, H. M. Chen, B. Liu, Ni^{3+}-induced formation of active NiOOH on the spinel Ni–Co oxide surface for efficient oxygen evolution reaction. *Adv. Energy. Mater.* **5,** 1500091 (2015).

48. C. L. McCrory, S. Jung, J. C. Peters, T. F. Jaramillo, Benchmarking heterogeneous electrocatalysts for the oxygen evolution reaction. *J. Am. Chem. Soc.* **135,** 16977-16987 (2013).

49. M. Yu, L. Jiang, H. Yang, Ultrathin nanosheets constructed $CoMoO_4$ porous flowers with high activity for electrocatalytic oxygen evolution. *Chem. Commun.* **51,** 14361 (2015).

50. C. Tung, Y. Hsu, Y. Shen, Y. Zheng, T. Chan, H. Sheu, Y. Cheng, H. Chen, Reversible adapting layer produces robust single-crystal electrocatalyst for oxygen evolution. *Nat. Commun.* **6,** 8106 (2015).

51. D. Xiong, W. Li, L. Liu, Vertically aligned porous nickel(II) hydroxide nanosheets supported on carbon paper with long-term oxygen evolution performance. *Chem. Asian J.* **12,** 543-551 (2017).

52. B. Zhao, L. Zhang, D. Zhen, S. Yoo, Y. Ding, D. Chen, Y. Chen, Q. Zhang, B. Doyle, X. Xiong, M. Liu, A tailored double perovskite nanofiber catalyst enables ultrafast oxygen evolution." *Nat. Commun.* **8,** 14586 (2017).

53. J. Suntivich, K. J. May, H. A. Gasteiger, J. B. Goodenough, Y. Shao-Horn, A perovskite oxide optimized for oxygen evolution catalysis from molecular orbital principles. *Science* **334,** 1383-1385 (2011).

54. S. Yagi, I. Yamada, H. Tsukasaki, A. Seno, M. Murakami, H. Fujii, H. Chen, N. Umezawa, H. Abe, N. Nishiyama, S. Mori, Covalency-reinforced oxygen evolution reaction catalyst. *Nat. Commun.* **6,** 8249 (2015).

55. Y. Zhu, W. Zhou, J. Yu, Y. Chen, M. Liu, Z. Shao, Enhancing electrocatalytic activity of perovskite oxides by tuning cation deficiency for oxygen reduction and evolution reactions. *Chem. Mater.* **28,** 1691-1697 (2016).

56. S. Zhao, Y. Wang, J. Dong, C. He, H. Yin, P. An, K. Zhao, X. Zhang, C. Gao, L. Zhang, J. Lv, J. Wang, A. M. Khattak, N. A. Khan, Z. Wei, J. Zhang, S. Liu, H. Zhao, Z. Tang, Ultrathin metal-organic framework nanosheets for electrocatalytic oxygen evolution. *Nat. Ener.* **1,** 16184 (2016).

57. Y. Han, J. Zhai, L. Zhang, S. Dong, Direct carbonization of cobalt-doped NH_2-MIL-53(Fe) for electrocatalysis of oxygen evolution reaction. *Nanoscale* **8,** 1033 (2016).

58. J. Duan, S. Chen, C. Zhao, Ultrathin metal-organic framework array for efficient electrocatalytic water splitting. *Nat. Commun.* **8,** 15341 (2017).

59. S. Chen, J. Duan, M. Jaroniec, S. Qiao, Nitrogen and oxygen dual-doped carbon hydrogel film as a substrate-free electrode for highly efficient oxygen evolution reaction. *Adv. Mater.* **26,** 2925-2930 (2014).

60. J. Tian, Q. Liu, A. M. Asiri, K. A. Alamry, Ultrathin graphitic C_3N_4 nanosheets/graphene composites: efficient organic electrocatalyst for oxygen evolution reaction. *ChemSusChem* **7,** 2125-2132 (2014).

61. R. F. Egerton, S. C. Cheng, Measurement of local thickness by electron energy-loss spectroscopy. *Ultramicroscopy* **21,** 231-244 (1987).

62. P. L. Zhang, L. Li, D. Nordlund, H. Chen, L. Z. Fan, B.B. Zhang, X. Sheng, Q. Daniel, L. C. Sun, Dendritic core-shell nickel-iron-copper metal/metal oxide electrode for efficient electrocatalytic water oxidation. *Nat. Commun.* **9,** 381 (2018).

63. A. J. Tkalych, H. L. Zhuang, E. A. Carter. A density functional + *U* assessment of oxygen evolution reaction mechanism on *β*-NiOOH. *ACS. Catal*. **7,** 5329-5339 (2017).

64. D. K. Bediako, B. L. Kaiser, Y. Surendranath, J. Yano, V. K. Yachandra, D. G. Nocera, Structure-activity correlations in a nickel-borate oxygen evolution catalyst. *J. Am. Chem. Soc.* **134,** 6801-6809 (2012).